Multifractal analysis for spatial characterization of high resolution Sentinel-2/MAJA products in Southwestern France

M. Neuhauser, S. Verrier, S. Mangiarotti

Multifractal analysis for spatial characterization of high resolution Sentinel-2/MAJA products in Southwestern France

M. Neuhauser[1], S. Verrier, S. Mangiarotti

CESBIO, Université de Toulouse, CNES/CNRS/INRAE/IRD/UPS, Toulouse, France

Highlights

- Particular scale breaks were detected on Sentinel-2/MAJA products
- Time variations in scaling regimes were noticed in series of surface reflectances
- The large-scale break was related to the landscape spatial structure
- The fine-scale break was explained by the effect of the optical acquisition system

Abstract

Multifractal analysis was applied to evidence spatial properties, in particular scaling behaviour, of Sentinel-2 surface reflectances and optical indexes acquired over the Southwest region of France. Considering the significant impact of clouds on the spatial properties of optical products, no study to our knowledge has focused on the multifractal analysis of a series of images. Images with minimal cloud cover were identified for the whole year 2016 based on the MACCS-ATCOR Joint Algorithm (MAJA) cloud and shadow detection process. This allowed us to access the dynamics of the scaling properties of surface reflectances, contributing to demonstrate the potential of multifractals for spatial characterization. Different scaling regimes, separated by significant scale breaks, were evident in these data. Through simulations from the Universal Multifractal model, we could explain the scaling properties and especially the position of scale breaks observed in the images studied by two types of phenomena. First, a transition scale located between hundreds of meters and one kilometre was detected on power spectra, structure functions and statistical moments. This specific scale was related to the average size of the agricultural plots of the studied region, revealing the direct link between the scaling behaviour observed and the physical properties of the surface. Second, an instrumental phenomenon was detected on the power spectra, resulting in a systematic transition scale observed near the resolution of the sensor and revealing the impact of the acquisition system on the high frequencies of optical images. In this research work, theoretical and/or empirical validation arguments

[1] Corresponding author : mathis.neuhauser@gmail.com (M. Neuhauser)

were provided as to the origin of the scales detected, contributing to demonstrate the value of multifractals to extract image texture from surface reflectance products.

Keywords

Surface reflectances; Optical indexes; Spatial characterization; Universal Multifractal; Sentinel-2; MAJA

1 Introduction

The last generation of space-borne sensors enables the acquisition of Earth surface information with both high temporal and spatial resolutions, showing good capabilities for studying environmental and anthropogenic evolutions at local to global spatial scales (Gutman et al., 2008; Huang et al., 2010). Among others, the most popular may be the U.S. Landsat-8 (Roy et al., 2014) and the recent ESA Sentinel-2 mission (Martimort et al., 2007) satellites. They provide multispectral images at spatial resolutions of tens of meters with a revisit time ranging between 5 and 16 days. Thanks to the benefits of their thirteen spectral bands, Sentinel-2 satellites (S2) deliver surface reflectances acquired from visible to short-wave infrared, allowing observation of a strong spatial variability in quite a wide range of wavelengths (Sotian et al., 2019).

Spatial heterogeneity is often closely linked to the temporal dynamics which itself relies on both natural phenomena associated with specific environmental conditions (meadows, forested areas, bare soils, etc.), and anthropogenic phenomena resulting from urban activities, agricultural practices, etc. Because these factors are present at different space scales and may have different spectral signatures, the information contained in acquired surface reflectances can be entangled in a very complex way and difficult to analyse from an image processing stand point (De Cola, 1989; Lam, 1990). Depending on the targeted applications, different techniques have been developed and used so far, to classify, model or characterize the land surface spatial and temporal properties with the aim to account for its complexity. In image classification, commonly used methods are based on the spectral signature of the observed scene (Lu and Weng, 2007), some of them involve complex data processing algorithms such as decision trees or neural networks (Hansen et al., 1996; Pal, 2005; Paola and Schowengerdt, 1995). In object-oriented classifiers, segmentation techniques make use of the spatial context of each pixel to improve the classification performance (Benz et al., 2004; Zucker, 1976). An embedding approach insensitive to the initial conditions was also introduced recently (Mangiarotti et al., 2018). For the modelling of the land surface, most of the developments have been based on optimization and data-assimilation techniques with the aim to improve the integration of remote sensed data into land surface process models (Bach and Mauser, 2003; Mangiarotti et al., 2008; Rodriguez-Fernandez et al., 2019). Using the global modelling technique, the first chaotic attractor directly issued from satellite data was obtained that illustrates the high complexity of the surface dynamics at large scale (Mangiarotti et al. 2012; 2014) and which itself relies on the level of spatial synchronization (Mangiarotti et al. 2016). To have a better description of the landscape changes, various linear and nonlinear characterization methods were introduced to describe the spatial variability of land surface (Gustafson, 1998; Puissant et al., 2005), some of them taking the spatial scale into account in their analyses (Mangiarotti et al., 2010, 2012). However, a more systematic spatial characterization requires

a statistical framework able to describe variability and image texture over a wide range of spatial scales. Statistical approaches like the Fourier power spectrum and entropy (Weszka et al., 1976) or variogram and fractal dimension (Ramstein and Raffly, 1989) can give relevant information on the spatial texture of the image such as roughness, autocorrelation, or the noisy nature of the signal for example.

Fractal analysis can be a relevant tool to quantitatively characterize the high degree of complexity and the spatial structure of surface products (Verrier et al., 2020) such as new remote sensing reflectances similar to S2 products (Alonso et al., 2017). Indeed, S2 products can be seen as images that embed a hierarchy of spatial structures of different sizes and of different energy levels. Many remote sensing images of natural variables show a fractal structure that can be demonstrated by various geometrical and statistical tools (Lovejoy et al., 2001; Qiu et al., 1999; Schmitt et al, 1993; Tessier et al., 1993). Studying such scaling features can contribute to identify specific set of scales on which specific properties apply. Kim and Barros (2002a) used such scaling analysis to characterize space-time variability of remotely sensed soil moisture and relate it to landscape characteristics (terrain, soil, vegetation). Two scale ranges were identified, a large one related to the hydrometeorological conditions (evapotranspiration, precipitation processes) and a fine one related to the soil properties of the surface (texture, structure). Precisely knowing these sets of scales aims to improve land surface modelling, considering both natural phenomena like topography, streams or drainage basins (Aguado et al., 2014; Cheng et al., 2001; Lyu et al., 2017) and anthropogenic phenomena like urban growth (Chen and Wang, 2013; Tan, 2021) or irrigation (Ko et al., 2016). Specifically, in hydrology these scaling features led to the development of better calibrated downscaling algorithms applied to surface soil moisture (Kim and Barros, 2002b; Ko et al., 2016; Mascaro et al, 2010; Neuhauser et al., 2019) and precipitation (Gires et al., 2012; Rebora et al., 2006).

One of the major constraints when measuring surface reflectances from space is the atmosphere. The latter is composed of different elements which have direct impact on reflectances. Indeed, clouds, gas molecules and aerosols are responsible for scattering and absorbing effects on the sun light reflected by the surface (Fraser et al., 1985; Vermote et al., 1997). These atmospheric components must be taken into account when analysing optical images, especially since they can affect the scaling properties of the signal measured from space. For example, several works have shown the fractal (and multifractal) behaviour of clouds acquired from visible and infrared sensors (Lovejoy et al., 2001; Siebesma and Jonker, 2000; Tessier et al., 1993).

Thus, in order to avoid the impact of clouds, most of the scaling studies of surface reflectances have been applied to images specifically chosen to be cloud-free (Alonso et al., 2017; Lovejoy et al.,

2008b). While these works prove the ability of multifractal analysis to investigate the scaling properties of images of surface reflectances, no seasonal properties/differences were really explored yet. Moreover, multifractal models were initially developed for modelling turbulence and atmospheric processes (Parisi and Frisch, 1985; Schertzer and Lovejoy, 1987), leading to many studies on atmospheric dynamics (Lovejoy et al., 2008a; Lovejoy and Schertzer, 2010c) but many fewer on continental surface characteristics.

Recently, with the increasing use of spaceborne optical sensors, several algorithms have been developed to take into account the effects of the atmosphere on the reflectances measured by satellite (Hagolle et al., 2010; King et al., 1999; Liang et al, 2001; Rahman and Dedieu, 1994). One of the most recent is the MACCS-ATCOR Joint Algorithm, called MAJA. It relies on the MACCS (Multi-sensor Atmospheric Correction and Cloud Screening) method – dedicated to aerosol optical depth estimation, clouds detection and atmospheric corrections (Hagolle et al, 2015; Lenoble et al., 2007; Rouquié et al., 2017) – and includes characteristics from the ATCOR algorithm (Atmospheric and Topographic Correction; Richter et al., 2006) such as the correction of slope effects. This processing chain is used within the French THEIA land data center (http://www.theia-land.fr) on multispectral images from Landsat-8, S2 and from the recent Venμs satellite (Manivasagam et al., 2019).

Considering this context, key scientific questions still need to be addressed in the field of spatial characterization of surface reflectances. The research work described here was realized in order to deepen our understanding of multifractal analysis and, above all, to demonstrate its value for improving spatial characterization of land surfaces. A particular reflection was made on the physical origin of the specific scales identified, relating them to image texture and asking whether the latter were due to:

- The seasonal specificities of the surface?
- The geographic specificities of the surface?
- The signal acquisition system of the satellite sensor?

To answer these questions, we investigated the occurrence of scaling properties in surface images collected by S2 sensors and corrected by MAJA. The dataset consists of S2-MAJA maps located in France at different dates within 2016. This research work was first focused on the southwestern region of France, on which a selection of particular dates was made to minimize the impact of clouds. In this region, particular consideration was given to the temporal dynamics of scaling properties due for example to seasonal effects. In addition, other regions of France with a different land use were then selected to investigate the impact of geographic specificities on the scaling properties. For each selected map, we analysed and compared the scaling properties of S2 images acquired in blue (B2),

green (B3), red (B4), near infrared (B8) and short-wave infrared (B11, B12) bands. The latter were chosen considering their strong relation with Earth surface physical and biophysical processes and their common use in previous studies involving multifractal analysis of surface reflectances (Alonso et al., 2017; Lovejoy et al., 2008b). The several bands of S2 sensors enable to explore the possible impact of the acquisition wavelength on scaling behaviour. Moreover, vegetation and soil moisture indexes obtained from these bands were also analysed to investigate how the combination of such bands can impact the scaling laws. This research study was done by applying multifractal analysis methods in the framework of the Universal Multifractal model (Schertzer and Lovejoy, 1987).

2 Case study and data

2.1 Study area

Southwestern France is a highly anthropized site, mainly composed of agricultural land. More than half of the ground area is exclusively dedicated to the development and management of crops throughout the year. Among the most common are sunflower, corn, wheat, barley, soybean and rapeseed crops. Considering also the urban areas which constitute ~ 2% of the landscape, the Southwest region has a spatial structure which is largely characterized by anthropic factors. These have an impact on the spatial heterogeneity of physical and biophysical variables such as surface temperature, soil moisture or vegetation. Natural factors also play a significant role in the spatial structuring of this landscape and its related processes, such as, for example, natural grasslands and forests (~ 10% of the surface) (Baup et al., 2015; http://osr-cesbio.ups-tlse.fr/~oso).

The climate in this region is temperate, inducing seasonal effects that impact significantly the temporal dynamics of surface variables. Springs are characterized by heavy rain, and summers are hot and dry with temperatures often reaching 35 °C (Battude, 2017). These climatic conditions have a direct effect on the landscape structure, more particularly on the evolution of this structure over the seasons. Indeed, the crop cycles – described by harvest and sowing periods – contribute to modify the heterogeneity of the surface as the seasons go by. In addition, the differentiation between winter and summer crops implies that not all crops have the same seasonal evolution and do not affect the landscape structure in the same way over time.

The study area is part of a French observatory, named Regional Spatial Observatory (RSO) and labelled by the French National Institute of Sciences of the Universe (INSU) since 2007. The purpose is to answer scientific questions related to the functioning and evolution of continental surfaces, but also to deal with more applied issues related to land use planning and sustainable management of resources (Dejoux et al ., 2012). In order to ensure this, both in-situ (Béziat et al., 2009; Burel, 2018; Tallec et al., 2013) and remote sensing observations (Baup et al., 2012) are combined. Thanks to these data, several works related to crop monitoring by remote sensing have been carried out in this region such as the study of wheat and rapeseed (Fieuzal et al., 2013) or even the estimation by agro-meteorological model of crop yields such as sunflower (Fieuzal and Baup, 2015), soybean (Baup et al., 2015; Betbeder et al., 2016) and corn (Fieuzal et al., 2017). These studies also allowed the preparation of recent space missions such as Venμs or S2, subsequently leading to high spatial resolution modelling of biomass and crop yields by optical data (Ameline et al., 2018; Battude et al., 2016; Claverie et al., 2012). The optical products from these new satellites now benefit from particular attention in this

region, since they are made available on the THEIA platform (http://www.theia-land.fr), corrected for atmospheric effects by the MAJA processing chain.

Due to the heterogeneity of its surfaces and the growing number of data acquired at various spatial scales, southwestern France is particularly well suited to the application of multifractal analysis tools such as those we used in this study. In this context, the present work consists of the analysis of MAJA-corrected surface reflectances acquired in the region of the 30TYP S2 tile (according to the tiles format and nomenclature provided by ESA; Gatti and Naud, 2017) whose spatial extent is shown in Figure 1. More specifically, our study was focused on a smaller study area of 40 x 40 km² covering part of the Gers French department (red square in Fig.1) and located within the 30TYP tile. This area in the Gers was chosen due to the predominant place of agricultural surfaces, limiting the impact of urban areas (cities, roads) on the spatial variability of physical and biophysical processes. In addition, due to certain constraints related to analysis tools (sample size, computation time) and cloud cover, we deliberately chose our study area by selecting a smaller zone than the area corresponding to the 30TYP tile which covers an area of 100 x 100 km².

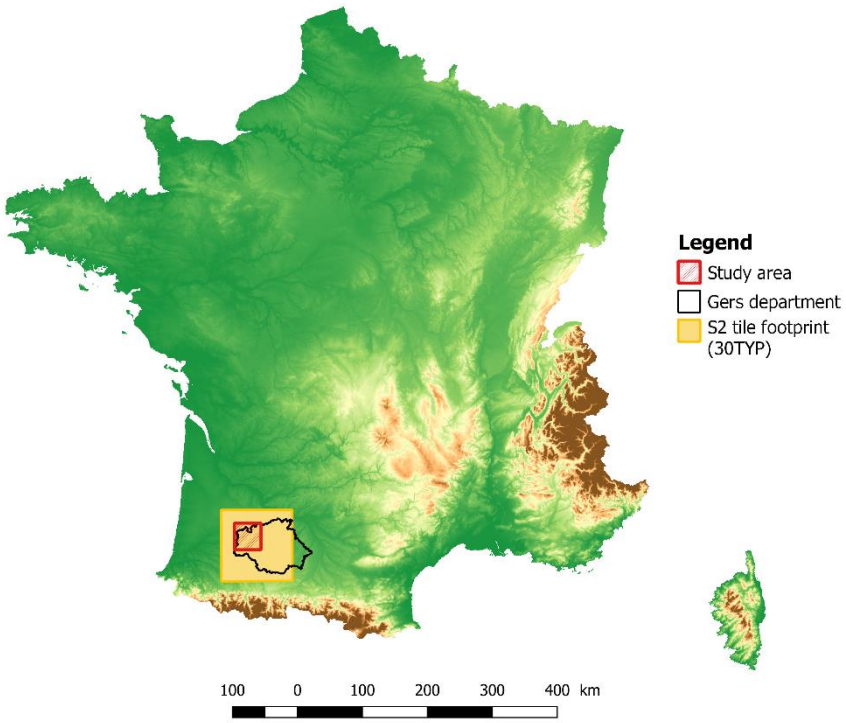

Figure 1 : Study area in the Southwest region of France.

This study investigates the period extending from January to December 2016, using the Sentinel-2A satellite. With a ten-day revisit time, S2A provides a sufficient temporal frequency to analyze the global temporal dynamics of the properties of continental surfaces over an entire year. Finally, we can also point out that the Southwest region has a relatively low average cloud cover throughout the year

compared to other regions of France located further north and south. Considering the impact of clouds on optical products, this criterion is not negligible in the choice of the study area.

2.2 Sentinel-2/MAJA products

We analyzed surface reflectances acquired in six spectral bands by the S2-A Multi-Spectral Instrument (MSI; Martimort et al., 2007) and then corrected by the MAJA chain within the CNES processing center (Centre National d'Etudes Spatiales; https://theia.cnes.fr). The selected bands are: three bands in the visible domain – blue B2 (0.50 µm), green B3 (0.56 µm), red B4 (0.66 µm), one band in near infrared B8 (0.84 µm) and two bands in the short-wave infrared B11 (1.6 µm) and B12 (2.2 µm). Note that all these bands are defined at 10 m resolution (in terms of pixel size) except B11 and B12 which are defined at 20 m resolution. The six bands were chosen because of their important link with the physical and biophysical processes of continental surfaces. The visible/near infrared has already been the subject of studies aimed at transcribing the fractal (De Cola, 1989; Lam, 1990; Qiu et al., 1999) and multifractal (Alonso et al., 2017; Lovejoy et al., 2008b) properties of continental surfaces.

In addition to reflectances, two optical indexes were also studied: the Normalized Difference Vegetation Index (NDVI; Tucker and Sellers, 1986) and the Normalized Soil Moisture Index (NSMI; Lampkin and Yool, 2004), which respectively account for the condition of the vegetation and the level of soil moisture. Since these variables are frequently used to investigate the functioning of continental surfaces, it is important to study their scaling properties. NDVI is constructed from surface reflectances (ρ) in the red (band B4) and near infrared (B8) wavelengths. NSMI is obtained from the combination of the bands in short-wave infrared B11 and B12:

$$\boldsymbol{NDVI} = \frac{\rho_{\boldsymbol{B8}} - \rho_{\boldsymbol{B4}}}{\rho_{\boldsymbol{B8}} + \rho_{\boldsymbol{B4}}} \qquad (\boldsymbol{10\ m}) \tag{1}$$

$$\boldsymbol{NSMI} = \frac{\rho_{\boldsymbol{B11}} - \rho_{\boldsymbol{B12}}}{\rho_{\boldsymbol{B11}} + \rho_{\boldsymbol{B12}}} \qquad (\boldsymbol{20\ m}) \tag{2}$$

These indexes are built in a non-linear way from reflectances in individual spectral bands, and it is interesting to check if (and how) potential scaling properties of ρ could result in scaling properties of the indexes.

Cloud masks from MAJA were used to identify images with less than 15% cloud cover. Fifteen dates were then selected over 2016 in order to limit the impact of clouds on surface reflectances and their scaling properties. These dates are shown in the chronogram in Figure 2, where we can see a distribution of dates that covers all seasons, with a larger number of images in summer. For the fifteen images, an average cloud cover of 2% was estimated over the period, with only 4 dates having more than 2% of clouds – the largest cloud cover being obtained on June 23 with 12.5%. Each of the remaining cloud pixels in the selected images were considered as missing data and were interpolated by bilinear interpolation. Note that no missing data other than that related to clouds was observed in our data, and that the corresponding size of the selected images are 4096 x 4096 pixels and 2084 x 2048 pixels respectively for 10 m and 20 m resolution products.

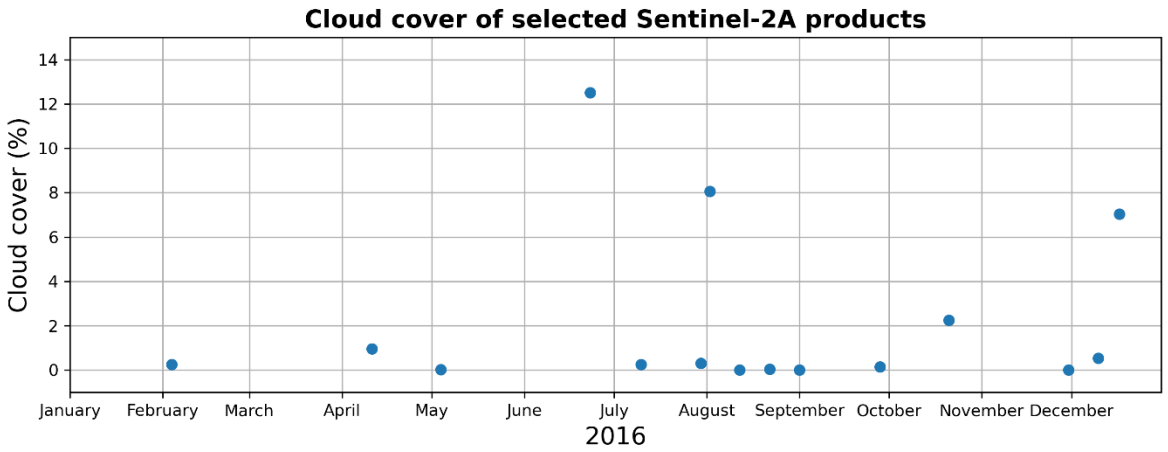

Figure 2 : Cloud cover of Sentinel-2A products selected over the January-December 2016 period, and corrected for atmospheric effects by MAJA. The corresponding dates were selected with less than 15% cloud cover.

3 Multifractal analysis methodology

During the last century, researchers realized that many geophysical processes could present scale invariance or scaling properties (Kolmogorov, 1941; Mandelbrot, 1967; Richardson, 1922). Multifractal analysis makes it possible to highlight these scaling behaviours, enabling spatial characterization of surface processes. To do this, several scale sensitive statistical estimators are applied to the surface reflectances acquired by satellite sensors. These estimators can be the power spectrum, the structure functions or the statistical moments. Different multifractal models, like the Universal Multifractal model (Schertzer and Lovejoy, 1987), are used to parametrize the scaling properties obtained from the statistical estimators. In this paper, a focus was made on one estimator, the power spectrum, which has the advantage to detect, in an easy and rapid way, some spatial properties of geophysical variables over different space scales (Lovejoy et al., 2008b). Structure functions and statistical moments (in the framework of Universal Model parametrization) were also investigated in this work. Since they confirm the properties already observed by power spectra, and for sake of simplicity and clarity, the theory and the methodology relative to these estimators are not presented in this part but are detailed respectively in Appendix A and B. More generally, we invite the reader to refer to Appendix A for a deeper understanding of the theoretical framework of fractals and Universal Multifractal model.

Because our study treats time series of satellite images, the statistical estimators will be computed for each image available during the studied period. Therefore, from this analysis two types of spatial characterization will be studied: (1) a mean characterization resulting from the average of individual estimators computed within the period, and (2) a “date by date” characterization of each image, allowing us to have access to the temporal evolution of the scaling properties of the products studied. For the calculation of estimators, note that, since only satellite images will be treated in this study, we will focus on the two-dimensional versions of the following techniques.

3.1 Vocabulary : scale and resolution

For the sake of clarity, we primarily want to define the terms "resolution" and "scale" within the meaning of fractal mathematical formalism. Indeed, although their meaning is close to that usually used by geophysicists, in particular in remote sensing, it can be appreciably different and could lead to certain misinterpretations in the remainder of this paper.

If we consider a space of (geometric) dimension $D = 2$ discretized over a set of intervals or pixels, the resolution λ of any fractal entity can be defined as the number of pixels present along a dimension of space. In the case of a satellite image of size 4 x 4 pixels, the resolution of the fractal entity is therefore equal to $\lambda = 4$ (Fig.3). Inversely proportional to the resolution, the scale l is associated with the size of a pixel and is defined according to λ:

$$l = \frac{L}{\lambda} \quad (3)$$

with L the extent or domain size along one dimension and corresponding to the greatest value of scale l. Unlike λ, the scale l is a dimensional variable (meters for an image). In the case of our 4 x 4 satellite image, the scale is $l = L/4$, which is the size of an elementary pixel. If we now aggregate our image on grids made up of new pixels twice as wide (or with an area four times as large), the resolution of the image will be taken equal to $\lambda = 2$, and the scale will be $l = L/2$.

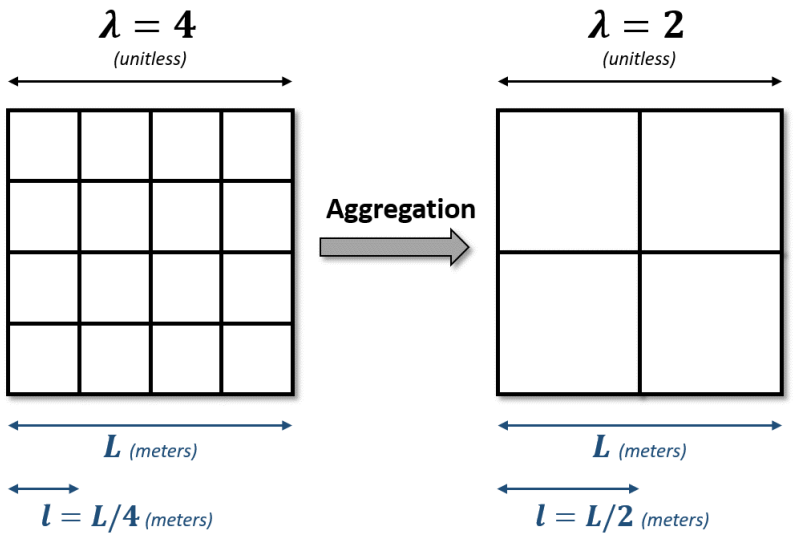

Figure 3 : Illustration of the concepts of resolution and scale from a two-dimensional fractal entity (satellite image).

In this way, any variable with fractal properties is defined on a continuum of resolutions (or scales) which extends from the finest resolution (to which is associated the smallest scale *i.e.* the size of an elementary pixel), to the coarsest resolution ($\lambda = 1$) corresponding to the largest scale ($l = L$).

In the following, scale sensitive statistical estimators will be called as “scaling estimators”, and will be computed on a spatial support represented either by resolutions λ, scales l, varying window size Δx or even spatial frequencies k, depending on the initial definitions of the estimators. Studying the evolution of surface products according to these spatial variables $(\lambda, l, \Delta x, k)$ provides access to fractal/multifractal properties that will be called hereafter as “scaling properties”. A scale range, corresponding to a set of scales with similar scaling properties, will be called as “scaling regime”.

3.2 *Power spectrum: evidence of spatial properties*

Power spectra are highly sensitive to the transition scales (also called “scale breaks”) that are located between scaling regimes characterized by different scaling properties. In a first step, the two-dimensional power spectral density $P(k_x, k_y)$ of the data under analysis, X, is estimated:

$$\boldsymbol{P(k_x, k_y) = |fft(X)|^2} \quad (4)$$

with P the power spectral density (PSD) defined on both vertical and horizontal image axes, corresponding respectively to k_x and k_y wavenumbers (spatial frequencies). Here, the estimation of the PSD is done through a two-dimensional fft or Fast Fourier Transform. Then, the more convenient one-dimensional isotropic angle-integrated power spectrum $E(k)$ is obtained (Lovejoy et al., 2008b; §8), that provides a 1D representation of the 2D fft power spectra:

$$\boldsymbol{E(k) = \int_{\|\vec{k}\|=k} P(\vec{k}) d\vec{k}} \quad (5)$$

where k is the modulus of the wavenumber and ||. || is the Euclidean norm. Since it expresses space frequencies, k is directly related to the spatial resolution λ. If the process presents scaling properties, the spectrum should follow a power law, where β is the negative slope of $E(k)$ on a log-log graph:

$$\boldsymbol{E(k) \approx k^{-\beta}} \quad (6)$$

The symbol “≈” indicates an equality within the limits of slowly varying functions. This method makes it possible to identify the range of scales (here the values of k) where there are scaling properties, and this through a first parameter called the “spectral exponent”.

3.3 *Scale break detection*

When analysing the scaling estimators, a segmentation algorithm (D’Errico, 2017) was systematically used to detect the scale breaks and thus the scale ranges in order to avoid subjective detections. This algorithm is based on the non-linear regression of "spline" curves (piecewise polynomial functions), making it possible to estimate the position of slope breaks within scaling estimators. It requires three input parameters: (1) the position on the x-axis of each point of the cloud to be segmented (support vector *i.e.* k, Δx or λ), (2) the value of each point on the y-axis (estimator vector such as E) and (3) the number of breaks nb_knots to detect. Once applied, the function outputs the position of the detected nb_knots breaks. Note that the number of breaks is a parameter which is therefore defined by the user. In order to check if the position is reliable and independent of the

312 number of breaks proposed, the algorithm was applied for several values of nb_knots ($nb\_knots =$
313 $1, 2, 3$), ensuring the same break was well detected in each case.

314

4 Results

4.1 Mean characterization over the period

Figure 4 shows the mean power spectra estimated over the full period (January-December 2016) of the different S2/MAJA products presented in Section 2. This represents an average spectrum based on individual spectra obtained within the period. Each spectrum is plotted in log-log coordinates, with the horizontal axis converted into spatial scale $l\ (= k^{-1})$ expressed in kilometres. The scale break detection algorithm identified two scale breaks common to all products: a first break l_1 located between a hundred meters and one kilometre, and a second break l_2 located on smaller scales. l_1 and l_2 positions are summarized in Table 1 for both surface reflectances and optical indexes.

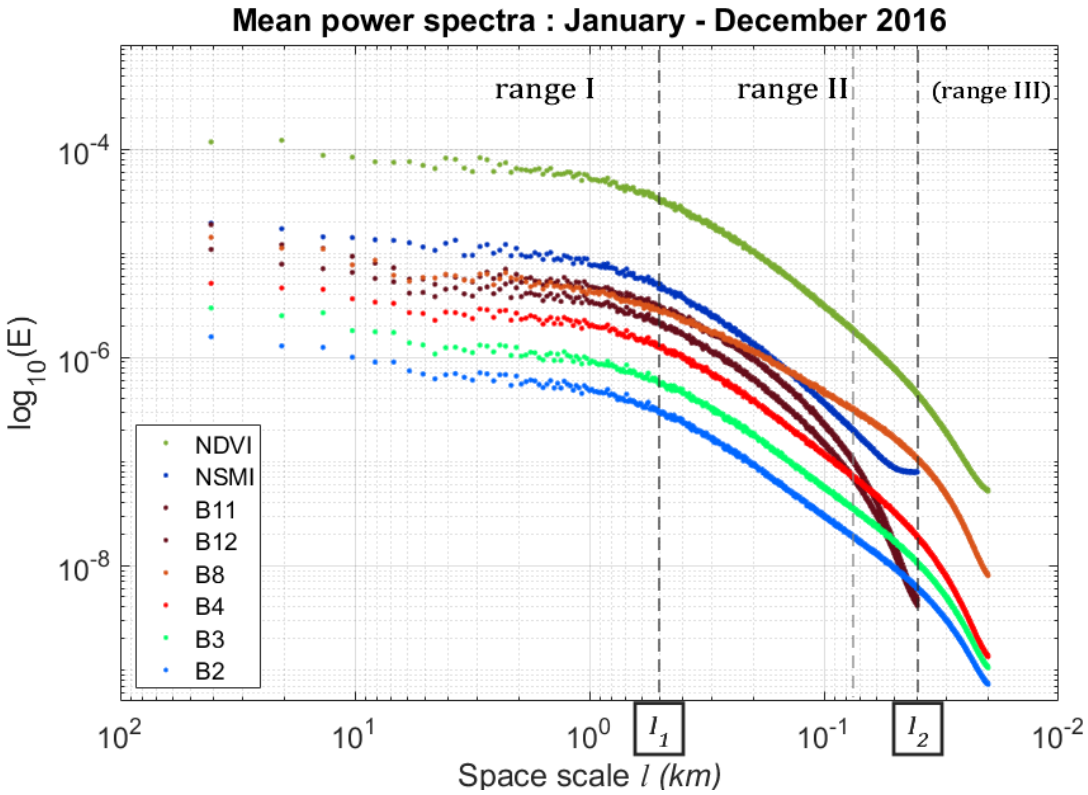

Figure 3 : Mean angle-integrated power spectra estimated from Sentinel-2 bands and indexes, over the period January-December 2016.

Considering all these products, the first scale break l_1 was estimated at about 400 m (computed from the geometric mean of individual breaks). The spectral slope β of each mean power spectrum (Table 2) was estimated for both ranges I ($l_1 > l$) and II ($l_1 > l > l_2$) (the last range (III) will be considered separately in Section 6). On *range I*, slopes are very close to zero and do not present significant differences within the different products ($0.2 < \beta < 0.3$). These results are in contradiction with those of Lovejoy et al. (2008b) who identified slopes greater than 1 ($\beta = 1.17 \pm 0.08$) on a similar

scale range (500 m – 25 km), from reflectances acquired in comparable spectral bands (MODIS sensor; Justice et al., 1998). Similarly, our results are also not comparable to those of Alonso et al. (2017) who observed only a single scaling regime over the range (120 m – 15 km), for reflectances from similar bands (Ikonos and Landsat-7 satellites). However, because of the different multifractal formalism used by Alonso et al. (2017), our spectral slopes and their results are difficult to compare. Nevertheless, Alonso et al. (2017) have indeed shown the presence of scaling properties over this range of scales. Thus, the differences between our results and those of Lovejoy et al. (2008b) and Alonso et al. (2017) can be linked to geographic specificities (central Spain in their cases) or to the fact that their analyzes were carried out on one or two particular dates, not allowing the acquisition of the scaling behaviour averaged over a period as we did here.

	Grid spacing (m)	SPECTRA		STRUCTURES	MOMENTS
		l_1 (m)	l_2 (m)	l_1 (m)	l_1 (m)
B2	10	420	37	580	360
B3		390	37	539	300
B4		390	39	555	360
B8		290	37	495	320
NDVI		380	48	575	340
B11	20	320	75	503	370
B12		370	75	565	390
NSMI		420	-	695	430

Table 1 : Positions of the scale breaks l_1 and l_2 estimated by segmentation (D'Errico, 2017) on mean Sentinel-2 power spectra, structure functions and statistical moments.

Regarding the behaviour of spectra on range II ($l_1 > l > l_2$), β values are greater than one and are relatively different between the products. The lowest slope value is estimated for the near infrared band ($\beta \approx 1.4$) and the greatest ones are found for the two short-wave infrared bands ($\beta \approx 2$). Considering visible bands (B2, B3, B4) and optical indexes (NDVI, NSMI), the β values obtained are between 1.6 and 1.8. We can also note in the spectra an increase of slope with the wavelength for reflectances acquired in visible domain.

As for the fine-scale break l_2, the latter is located at around 40 m for products with a resolution of 10 m (visible bands, near infrared band and NDVI) and is shifted towards larger scales (75 m) for products with a 20 m grid resolution (short-wave infrared bands B11 and B12). It even disappears with regard to the NSMI soil moisture index (flat spectrum for the fine scales). If we analyze this last

spectrum in more detail, a rise in the curve is observed towards the points located at the finest scales (~ 50 m). This rise reflects the presence of noise in the NSMI data which affects the highest frequencies of the image, artificially creating an excess of energy at fine scales. Since bands B11 and B12, from which the NSMI has been estimated, do not show such an increase in their spectra at fine scales, their combination must be the source of the noise observed on the soil moisture index at high frequencies. This phenomenon was expected since the ratio of two signals is known to contain more noise (due to a reduction in the signal to noise ratio). Similarly, we can note that the NDVI is characterized by a l_2 scale break (at 48 m scale) that is less pronounced than for the bands B3 and B8 from which it was generated, with a very slight rise of the spectrum for highest frequencies (scales close to 20 m). Although the phenomenon is much less pronounced than for the NSMI, the vegetation index also appears to be somewhat impacted by the combination of bands.

Continuing the comparison between bands and indexes, these results tend to show that on fine scales ($range\ II$) the vegetation index is characterized by an average spectral behaviour comparable to the band B4 (red) but different from band B8 (near infrared). However, the spectral slope of the soil moisture index is found to be close to those obtained from both of the short-wave infrared bands B11 and B12. Another general remark on the spectra can be made on the quality of the scaling law which is very good on $range\ II$, considering all products ($R^2 \approx 0.98$), while it is strongly reduced on $range\ I$ ($R^2 \approx 0.6$). This can partly be explained by the sampling of power spectra which is sparser on low frequencies (large scales) than on high frequencies (fine scales).

The results presented above were compared with the two other approaches (structure functions and statistical moments presented in Appendix B) and their results (figures in Appendix C) were found to be consistent with those of the power spectra. The positions of l_1 scale break obtained from these approaches are presented in Table 1, with the corresponding parameters detailed in Table 2 for both ranges.

(a)	Grid spacing	Scale range	β	R^2_β	α	C_1	$R^2_{K(q)}$	H	R^2_H
B2			0,30	0,62	1,96	0,007	0,89	-0,27	0,98
B3			0,31	0,64	1,86	0,006	0,91	-0,28	0,99
B4	*10 m*	*range I*	0,24	0,55	1,81	0,007	0,92	-0,30	0,99
B8			0,29	0,60	1,80	0,004	0,89	-0,27	0,99
NDVI			0,20	0,50	1,91	0,005	0,88	-0,31	0,99
B11			0,28	0,56	1,83	0,004	0,87	-0,29	0,99
B12	*20 m*	*range I*	0,25	0,53	1,81	0,005	0,88	-0,29	0,99
NSMI			0,22	0,55	2,23	0,005	0,83	-0,29	0,99

(b)	Grid spacing	Scale range	β	R^2_β	α	C_1	$R^2_{K(q)}$	H	R^2_H
B2			1,63	0,99	1,97	0,11	0,96	0,32	0,98
B3			1,67	0,99	1,78	0,11	0,96	0,32	0,98
B4	*10 m*	*range II*	1,76	0,99	1,56	0,12	0,96	0,35	0,97
B8			1,37	0,98	1,53	0,09	0,96	0,23	0,93
NDVI			1,84	0,99	1,61	0,13	0,96	0,37	0,98
B11			1,96	0,97	1,53	0,11	0,97	0,35	0,95
B12	*20 m*	*range II*	1,96	0,98	1,53	0,12	0,96	0,37	0,97
NSMI			1,81	0,98	1,97	0,11	0,96	0,35	0,98

Table 2: Scaling parameters obtained from multifractal analysis on $range\ I$ (a) and $range\ II$ (b) of Sentinel-2 products, over the period January-December 2016. The values of β, α, C_1 and H were obtained from linear regressions applied on mean statistical estimators. However, R^2 coefficients presented here corresponds to the average of all coefficients obtained on each date. Note that $R^2_{K(q)}$ is the average of the coefficients obtained on every moment curves. Similarly, H is obtained from the average of H_x and H_y, as R^2_H is obtained from R^2_{Hx} and R^2_{Hy}

4.2 Temporal and spatial variations of the scale breaks

Different scaling regimes were observed on the S2/MAJA products, separated by specific scale breaks: a first break l_1 detected on the scaling estimators between hundreds of meters and one kilometre, and a second break l_2 detected on the high frequencies of the mean power spectra. To explain the origins of these observations and their link with the spatial texture of the data, the evolution of these breaks was analysed according to the seasonal and spatial evolution of the surface.

To explore the seasonal evolution of the scale breaks l_1 and l_2, the scale break detection algorithm was applied on each individual spectrum obtained between January and December 2016 (*i.e.* spectra computed for each available image). The time series of l_1 (Fig.5.a) is found to be largely variable for all bands, whereas l_2 (Fig.5.b) presents a quite constant evolution during the period. Therefore, these

two scale breaks detected on power spectra seem to be of a different nature: on the one hand the large-scale break l_1 seems to be related to the seasonal evolution of surface processes, on the other hand the fine-scale break l_2 position is found to be relatively independent of time. In addition, we note that the ratio between l_2 and the minimum scale (that is to say the grid resolution of the image for a given band) is comparable considering both 10 m and 20 m bands: $l_2 \approx 4 \times l_{min}$. This relationship appears to be constantly present throughout the period.

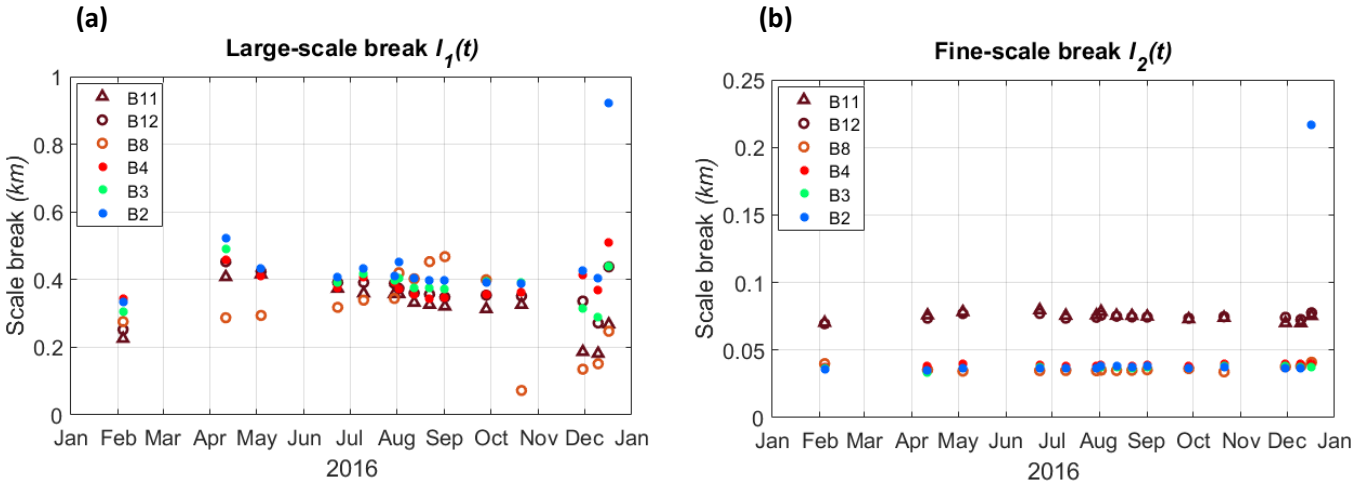

Figure 5: Time series of the position of the scale breaks l_1 (a) and l_2 (b) estimated from the power spectra of the Sentinel-2 bands, over the period January-December 2016.

To understand the origin of these two scales, it was investigated whether the geographic specificities related to the study area could have an impact on the position of these scale breaks. Since l_1 relies on the seasonal evolution of the surface, changes in land use should have an effect on the position of l_1, whereas they should not on l_2. To so investigate this question, several regions of France with a different land use were selected. These regions were identified using the land use products supplied by the Scientific Expertise Center for Land Use CES OSO (http://osr-cesbio.ups-tlse.fr/~oso). This analysis was done from the land use map for 2016, obtained from S2 products, and presented in Figure 6. In addition to the original tile (30TYP), five new S2 tiles were added to our study, corresponding to five types of surface or classes: *crops*, *forest*, *urban*, *vineyards* and *grasslands*. The areas were chosen so that the extracted S2 images contain for each class a majority of pixels belonging to the class in question. For the six zones, we extracted the surface reflectances acquired in two spectral bands defined at 10 m (B2, B8) at two dates in the year 2016 (summer, autumn). Table 3 specifies the position of the breaks l_1 and l_2 detected in the power spectra. In general, considering all the zones, bands and dates provided, these results show a break l_2 which varies between 32 m and 42 m, and a break l_1 which is between 72 m and 1 km. Therefore, the position of the large-scale break l_1 seems much more impacted by the type of surface, the date of acquisition and the spectral band (when it is defined according to the same spatial resolution) than the fine-scale break l_2.

These temporal and spatial behaviours confirm the different nature of the transition scales. In the following sections, demonstrations are made to relate these scale breaks with (1) the seasonal and geographic specificities of the surface in the case of the scale l_1 and (2) with the acquisition system of optical images for l_2.

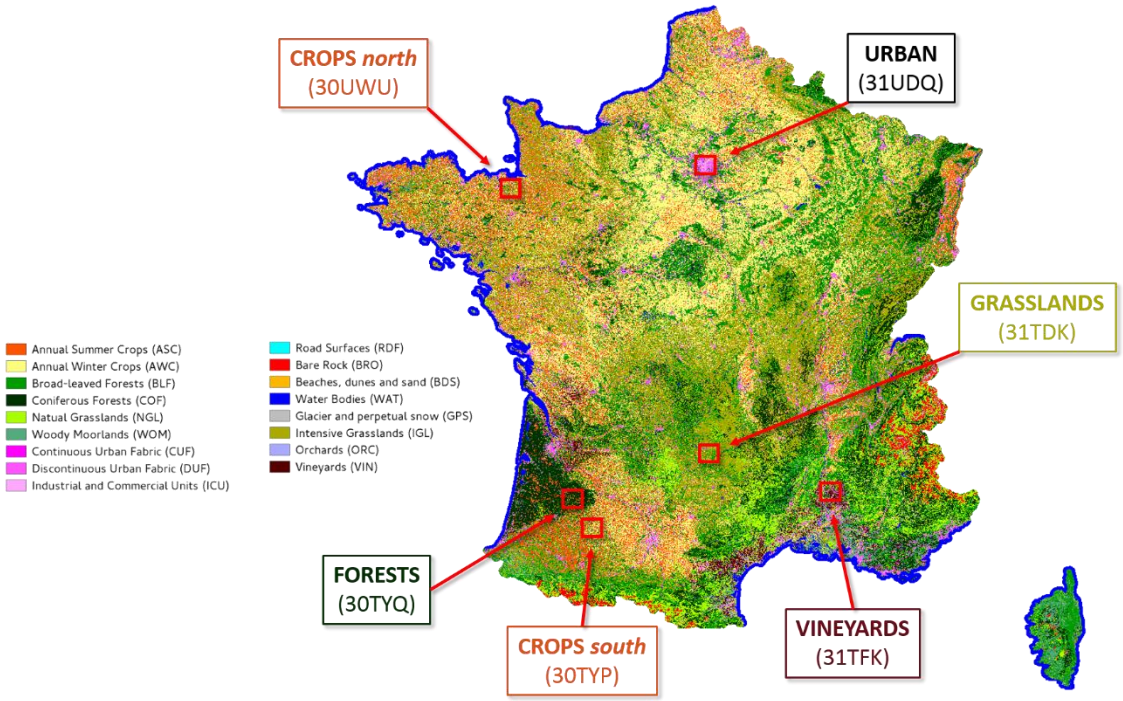

Figure 6: Six study areas corresponding to the five types of surface (crops, forest, urban, vineyards, grasslands) identified from the 2016 land use map of France CES OSO.

	Summer				Autumn			
	Band B2		Band B8		Band B2		Band B8	
	l_1	l_2	l_1	l_2	l_1	l_2	l_1	l_2
***crops** south*	440	36	340	35	390	37	72	34
forests	860	32	1000	39	910	34	210	38
***crops** north*	310	36	380	34	380	33	460	41
urban	-	40	-	42	-	39	-	40
vineyards	150	34	180	35	150	34	130	35
grasslands	280	37	350	34	140	37	250	37

Table 3: Positions (in meters) of the scale breaks l_1 and l_2 estimated from the power spectra corresponding to six types of surface, observed in bands B2 and B8, in summer and autumn 2016.

5 A large-scale break related to the seasonal and geographic specificities of the surface

5.1 Seasonal dynamics linked to crop cycle

To propose an explanation to the large-scale break l_1 between ranges I and II, first the temporal evolution of the scaling properties of the S2 products can be observed on the two ranges, for the studied period. The time evolution of the spectral exponent β estimated for the six bands (Fig.7) exhibits on the fine scale range $(range\ II)$ a seasonal cycle of the spectral slopes, while no particular behaviour is detected on large scales $(range\ I)$. In addition, the dynamics of the β values are much higher on fine scales $(0.8 < \beta < 2.4)$ than on large scales $(0 < \beta < 0.9)$.

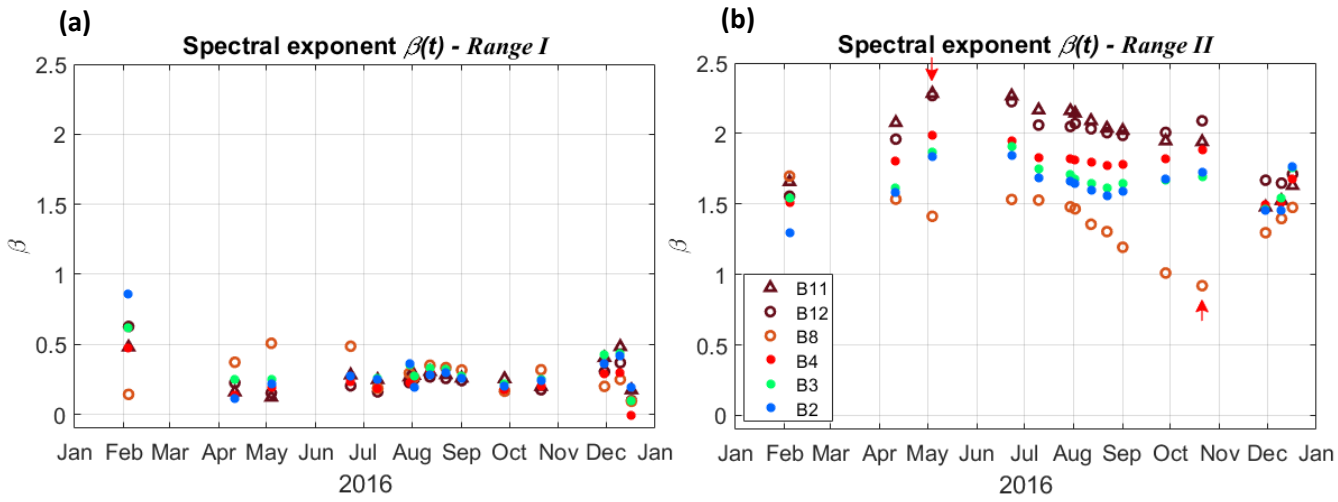

Figure 7: Time series of spectral exponents of the Sentinel-2 bands, over the period January-December 2016 for range I (a) and range II (b).

If we analyze in more detail the cycle observed on fine scales (Fig.11.b), the dynamic detected on the visible bands (B2, B3, B4) is characterized by minimum values in February, August and then December $(\beta \approx 1.5)$ and peaks of values around May-June then October $(\beta \approx 1.9)$. For the short-wave infrared bands (B11, B12), the maxima are placed at the same dates as for the reflectances acquired in the visible domain but they do not present the same intensity: the peak observed in May-June is very marked – with values reaching 2.3 (arrow on the graph) – while that of October is weaker (even almost non-existent for B11). Considering the near infrared B8 band, a reversed cycle is found on $range\ II$ (compared to the other bands), characterized by minimum values for the months of May-June and then October. In addition, the spectral exponent of B8 shows a much more marked dynamic in the second half of the period – values of β falling from 1.5 (July) to 0.9 (October, arrow on the graph) – than in the first half of the period $(1.4 < \beta < 1.7)$. Thus, for the month of October, the images acquired in the near infrared seem to lose spatial autocorrelation, with a spectral slope approaching zero. This temporal evolution of scaling properties is illustrated on Figure 8 where the individual power spectra of four near infrared images are compared: two images acquired in summer (July 10 and July

30) and two images acquired in autumn (September 28, October 21). For these spectra, the fine-scale break l_2 was estimated at around 35 m in all four cases, confirming its "instrumental" origin (see Section 6). On the other hand, two different l_1 breaks were obtained: at around 350 m for the July spectra (dark red and light red curves) and the September spectrum (light green curve), and at 72 m for October (dark green curve). It appears that the l_1 break in July moves towards fine scales in October, combining with l_2. Thus, these results show that a switch takes place from two scaling regimes in summer and early autumn to a single one in autumn. On this period, we observe the decrease of the spectral slope with time, confirming the evolution presented in Figure 7.b. For October 21, the regime seems to be found on a scale range close to the global range provided by our data (72 m – 41 km), and presenting a spectral slope less than 1.

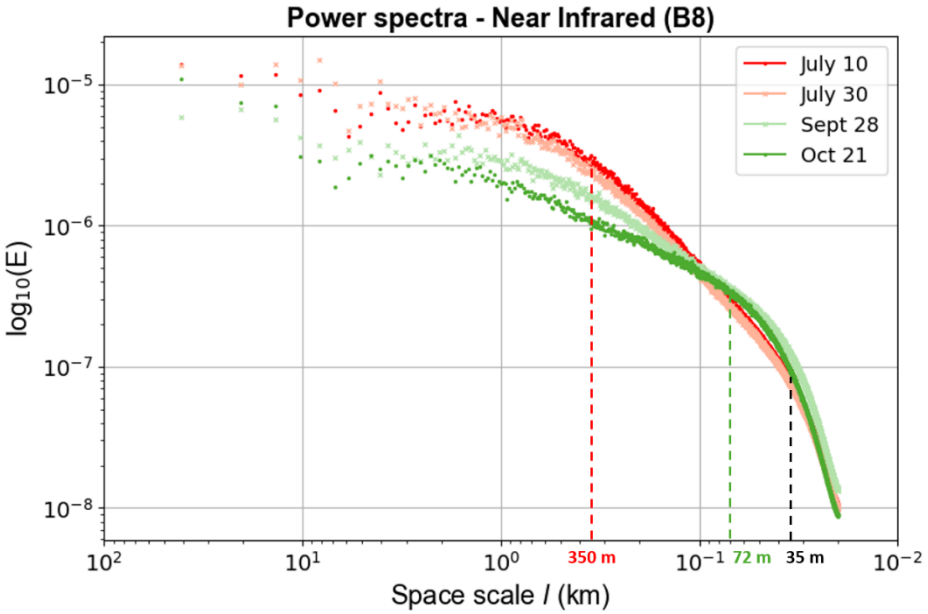

Figure 8: Power spectra of surface reflectances acquired in summer and autumn 2016 by the near infrared band B8.

These results confirm the link between the fine-scale break l_1 and the temporal and spatial variations of the surface. Therefore, considering the predominant place of agricultural surfaces in the study area, our hypothesis is that this time variation is related to the crop cycle (with the more abrupt changes associated with harvesting and sowing), taking place during the mid-season periods (autumn, spring). The evolution of crops, including the transitions between winter and summer crops, would explain the cycle that we detect here. This hypothesis can also explain the reverse nature of the cycles between near infrared and visible/short-wave infrared behaviours. Indeed, the reflectances acquired in the near infrared, being very sensitive to vegetation, should exhibit more spatial variability when

458 the crops are well developed, therefore for periods between the harvest and sowing phases. If we take
459 the example of corn, which is one of the main crops grown in Southwestern France, the harvesting
460 phase usually occurs between August and November. This corresponds to the fall observed on the β
461 parameter estimated from the band B8. Thus, a harvest phase would correspond to a loss of spatial
462 heterogeneity in these wavelengths, revealing a poorer and less structured signal than during a
463 vegetation growth phase. In addition, the gradual drop in spectral slope (beginning of decrease
464 observed from August) can be explained on the one hand by the staggering of the sowing phases
465 between August and November (according to the calendar of each farmer), and on the other hand by
466 the senescence phase occurring before harvest and helping to reduce the ability of vegetation to
467 reflect solar radiation (less chlorophyll). Conversely, visible reflectances behave differently by being
468 sensitive to other elements of the surface such as roads, buildings, or even the bare soil that appears
469 once harvesting is complete. Thus, at mid-season, when the vegetation has just been sown, the surface
470 shows more spatial variability in the visible than in the near infrared domain.

471 To develop the interpretation proposed above, our results were compared with some
472 characteristics of the surface, and more particularly with its spatial structure. The study area is mainly
473 composed of agricultural plots of which the majority reveals an area between 0.3 and 130 ha,
474 corresponding to a plot width (assuming square areas) of around 50 to 1000 m. This could be identified
475 thanks to the Graphic Parcel Register (GPR; https://geoservices.ign.fr) for the year 2016, allowing
476 access to the delimitation, the surface area and the type of crops of all the agricultural plots in the
477 department of Gers. An average plot width of around 170 m was deduced from this data. Figure 9
478 below shows a part of the GPR for our study area, for which the plots were classified according to their
479 extent. We observe a large number of plots whose characteristic widths are between 100 m and 1 km
480 (areas in light blue, green and yellow). Although the agricultural plots reveal quite different structures,
481 of more or less elongated shapes, even with rounded "edges", the more or less systematic cutting that
482 they generate on the surface could be at the origin of the large-scale break l_1 observed in our results.
483 In this way, the fine-scale regime observed on $range\ II$ would reflect the *intra-plot* variability
484 governed by multifractal physical and biophysical processes linked to crops (soil moisture, vegetation,
485 etc.), while the large-scale regime on $range\ I$ would represent the *extra-plot* variability resulting from
486 the aggregation of several fine-scale processes which together would not have particular multifractal
487 properties. This interpretation would explain the uncorrelated and less complex nature of the
488 reflectances on large scales (very low values of β and C_1 parameters on $range\ I$), whereas more
489 complex fractal and multifractal properties were obtained on $range\ II$ tending to justify the interest
490 of applying a multifractal model like that of Universal Multifractals on these fine scales.

Figure 9: Classification of agricultural plots (parcels) according to their surface area estimated from the Graphic Parcel Register for the year 2016. The data represented here correspond to an area of ~ 3 x 3 km² extracted in our main study area. The plot widths were calculated from the surface areas by approximating them to square areas.

491

492 ## *5.2 Simulation of the impact of agricultural plots on the scaling properties of surface*
493 ## *reflectances*

494 In order to check if the previous explanations are realistic, an example of agricultural area was
495 simulated with the same scaling properties as the S2 reflectances. To do this, a synthetic multifractal
496 field was simulated by applying the Universal Multifractal model (see Appendix D), to which we
497 combined an image containing the delimitations of agricultural plots obtained from the GPR-2016 on
498 our study area (Fig.10.a). The multifractal field was generated by defining the values of the universal
499 parameters of the model at $\alpha = 2$, $C_1 = 0.1$ and $H = 0.3$, corresponding to the values obtained for
500 the band B2 on $range\ II$ (mean behaviour, Table 2.b). The combination method simply consists in
501 adding the spatial texture generated by the agricultural plots to the image of the simulated multifractal
502 field. To reproduce a more realistic texture, the entities ("plot" objects) have been previously grouped
503 into six classes: the same pixel value between the min and max values of the initial field, *i.e.* 0 and 1,
504 has been assigned to each of these classes. These have been defined according to the area of the
505 entities: the plots have been grouped into object classes whose area is within a predefined interval.
506 Here, these intervals have been defined from the area quantiles, so as to have the same number of
507 objects in each class. Although this classification does not correspond in any way to reality, it allows to
508 reproduce artificially the differences in intensity of reflectances according to the type of soil (different

types of crop, bare soil, forest, etc.) which can be observed on the real data (Fig.10.b). The final surface generated (i_{agri}) is based on an integrated multiplicative cascade (i_{MF}) defined at all scales of the image, but to which is added the spatial texture of agricultural plots ($offset_{parcels}$) such as:

$$\boldsymbol{i_{agri} = i_{MF} + offset_{parcels}} \quad (7)$$

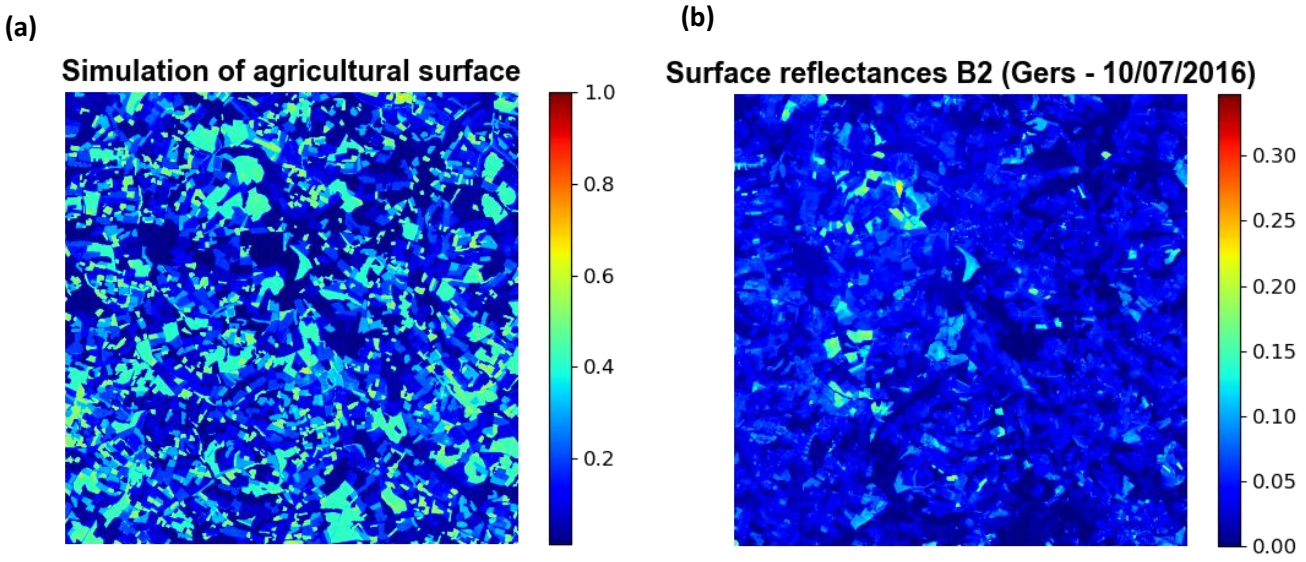

Figure 10: Simulated and real surface reflectances corresponding to the study area (Gers, 30TYP tile). The simulation was obtained by combining a multifractal field and the GPR of the year 2016.

The graph in Figure 11 represents the power spectrum obtained for the simulated agricultural surface $\mathrm{i_{agri}}$ (green curve), compared to that obtained from the original simulated multifractal field $\mathrm{i_{MF}}$ (blue curve). The power spectrum estimated from an image $\mathrm{i_{B2}}$ of real surface reflectances (gray curve) is also presented. $\mathrm{i_{B2}}$ is the image acquired in B2 band on July 10 (image presented in Fig.10.b). For the sake of clarity, the finest scale of the simulated fields was set to the size of a S2 pixel (band B2) so that $l_{min} = 10\ m$.

As expected, a single scaling regime is observed on the original multifractal $\mathrm{i_{MF}}$ with no scale break detected, whereas two scaling regimes are indeed observed for $\mathrm{i_{agri}}$, with a scale break l_1 detected at around 200 m. This break noticed on $\mathrm{i_{agri}}$ is located a few dozen scales higher than the finest scale, which is comparable to the results obtained from S2 data. The two regimes exhibit behaviours close to those observed on the ranges I and II of $\mathrm{i_{B2}}$, at least in terms of the shape of the curves. Indeed, on large scales ($range\ I$) a spectral slope smaller than 1 is obtained, while a spectral slope greater than 1 is estimated on fine scales ($range\ II$). Therefore, the twofold scaling behaviour of S2 products is clearly transcribed by our simulation : it was evidenced here that a definite link exists between the division of

the area by agricultural plots and the presence of two scaling regimes – with a transition scale which is effectively close to the average plot scale. We note a flattening at the finest scales of the i_{agri} power spectrum, which reveals the presence of noise localized on the last octave (20 m – 40 m). A similar flattening was observed on the NSMI spectrum (Fig. 4) due to the creation of noise by the application of the NSMI formula. For the i_{agri} spectrum, this phenomenon is probably due to the "local" effect of the boundaries of agricultural plots at resolutions close to the pixel size. Indeed, these boundaries generate abrupt transitions from one pixel of the image to its neighbour, leading to an increase of the energy at this specific scale. The fact that this flattening is observed on the simulated agriculture spectrum (i_{agri}) but is not on the real spectrum (i_{B2}) may be due to (1) the impact of our combination method creating artificial boundaries that are more abrupt on the simulation than on the real case, and/or (2) the impact of the optical acquisition system (Section 6) on the real spectrum which inversely affects the fine scales (slope increased) but that is not considered in this simulation.

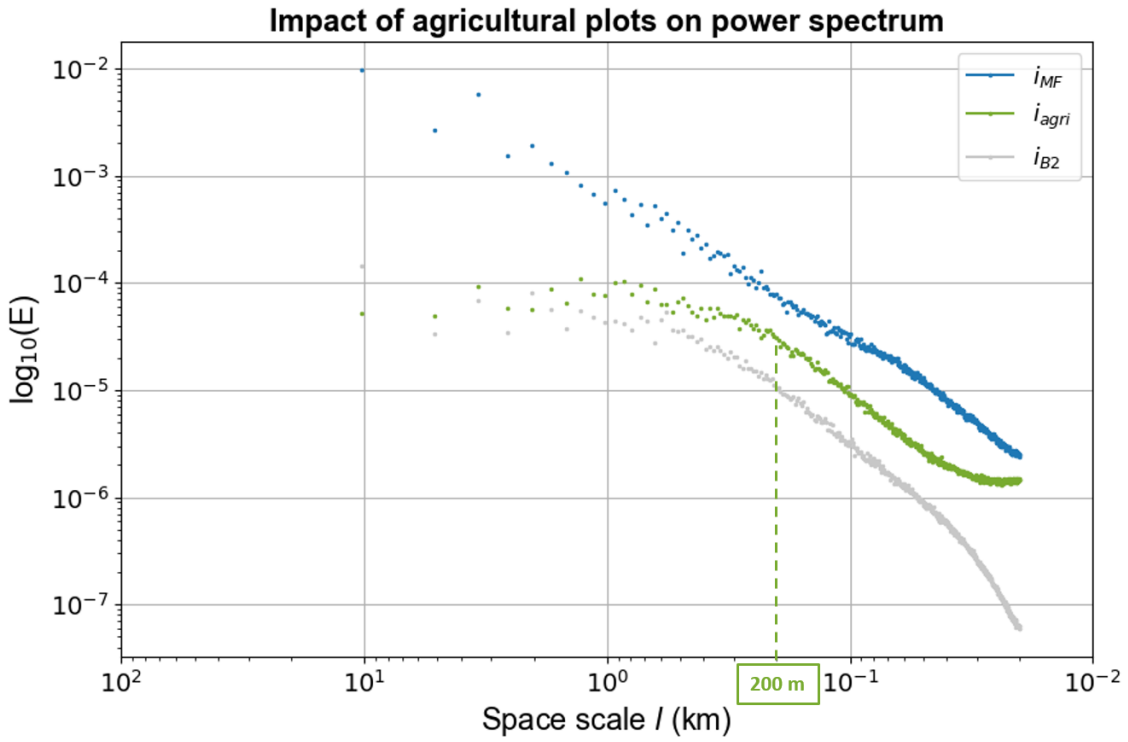

Figure 11: Impact of agricultural plots on power spectrum of simulated surface reflectances (Fig.10.a).

6 A fine-scale break related to the optical acquisition system of the satellite sensor

This section is dedicated to the interpretation of the scale break l_2 observed on power spectra between range II and III.

6.1 The effect of the Modulation Transfer Function

Considering the relatively small variations of the position of the fine-scale break l_2 with time and land use, this break could be a consequence of the acquisition system which affects the high spatial frequencies of images. In any optical system, this phenomenon is modelled by a function called MTF (Modulation Transfer Function; Norton et al., 1977). It defines the system ability to transmit the spatial frequencies of the observed scene. It is affected by several components of the system such as the objective (the lens) and detectors, but also by external factors such as temperature or atmospheric diffusion. During the satellite launch in space, these last factors can modify the MTF. However, the latter varies very little over time once the satellite is finally placed in its orbit. In this way, it could be the reason for the systematic break observed at the maximum frequencies acquired by the MSI-S2 sensor.

As part of the validation and calibration procedures for S2 products, Gascon et al. (2017) determined the modulation transfer function of the MSI imager after the launching of the S2-A satellite. This has been estimated from an image acquired in the B2 band on Arizona (USA), applying the "slanted-edge" method (Viallefont-Robinet and Léger, 2010; Reichenbach et al., 1991) which has often been used to determine the MTF of space sensors like Landsat (Carnahan and Zhou, 1986) or Ikonos (Choi , 2002).

6.2 Simulation of the impact of optical acquisition system on scaling properties

Given what has been described above, we made the hypothesis that the scale break l_2 detected on the power spectra is directly related to the impact of the MTF on the scaling properties of the “original” signal acquired by the MSI sensor.

To demonstrate this, a multifractal field was simulated (according to the method presented in Appendix D which is based on the Universal Multifractal model) representing the scaling behaviour of a hypothetical original signal, *i.e.* with fractal/multifractal properties not impacted by the optical system. Here, we suppose that the original signal should have the same scaling properties as those obtained on $range\ II$ (Figure 4), with parameters set as $\alpha = 2$, $C_1 = 0.1$, $H = 0.3$ (values obtained from band B2, Table 2.b). Note that we did not consider in this simulation the impact of agricultural plots (Section 5.2).

Then, to simulate the impact of optical acquisition system, we generated an MTF according to the model of Viallefont-Robinet and Léger (2010). The latter proposed a parametric model taking into account various characteristics of the system such as the diffraction effects of the lens and the sampling effects of the detector, as well as the impact of other factors such as the displacement of electronic charges or correction of the focus that can be achieved after launching the satellite. Here, for the sake of simplicity, only the major effects on MTF have been taken into account, namely diffraction and sampling. Finally, this function was applied to the simulated multifractal field. The operation was carried out in the Fourier domain by applying the following relation:

$$\boldsymbol{I_{filtered} = MTF \times I_{simu}} \quad \textit{8}$$

with $\boldsymbol{I_{filtered}}$ and $\boldsymbol{I_{simu}}$ the Fourier transform modules of the images corresponding respectively to the field filtered by MTF and to the simulated original field.

For the calculation and generation of the MTF, the equations used are detailed in Appendix E. Two parameters are to be defined in the model: (1) the sampling frequency f_s of the detector which was fixed here at the resolution of the simulated multifractal field, that is, at 1 pixel^{-1} (here, the scale is expressed in pixels, the corresponding unit is thus "pixel^{-1}" for frequency), (2) the cut-off frequency f_c of the lens (also defined at 1 pixel^{-1} for the sake of simplicity) which is responsible for the diffraction effects. In reality, the value of f_c depends on the characteristics of the lens (diameter, focal length) and on the wavelength of the incident radiation. However, since we did not have access to the value of the MSI sensor focal length, we were unable to determine the actual cut-off frequency. According to Gascon et al. (2017), the MTF they measured for band B2 has a value close to 0 at the sampling frequency. This shows that, for this band, f_c should be positioned close to f_s, at slightly higher frequencies. According to this assumption, we will suppose thereafter that $f_s \approx f_c = 1$ pixel^{-1}.

Figure 12 presents the power spectra of the original field (blue curve), of the field affected by the MTF by considering only the sampling effects of the detector (dark brown curve), only the diffraction effects of the lens (light brown curve), and finally by considering both the sampling and diffraction effects (red curve). For the sake of clarity, the scale axis of the figure was adapted to correspond to that of S2 spectra: the finest scale of the fields was set to the size of a S2 pixel (band B2) so that $l_s = \frac{1}{f_s} = 10\ m$. The fine scales are found to be impacted by the MTF the more significantly: the energy of the signal is attenuated for the high frequencies, resulting in an increase in the spectral slope for scales lower than 100 m. This behaviour is obviously more pronounced when the two effects (diffraction and sampling) are combined (spectrum in red). The scale break detection algorithm (Section 3.3) was applied on this last spectrum, which revealed a scale break located at 48 m ($= 4.8\ l_s$). The relationship

found here between the position of the break and the resolution of the image is comparable to that deduced from our S2 products, for which the coefficient linking the two scales was close to 4 over the entire period (Fig.5.b).

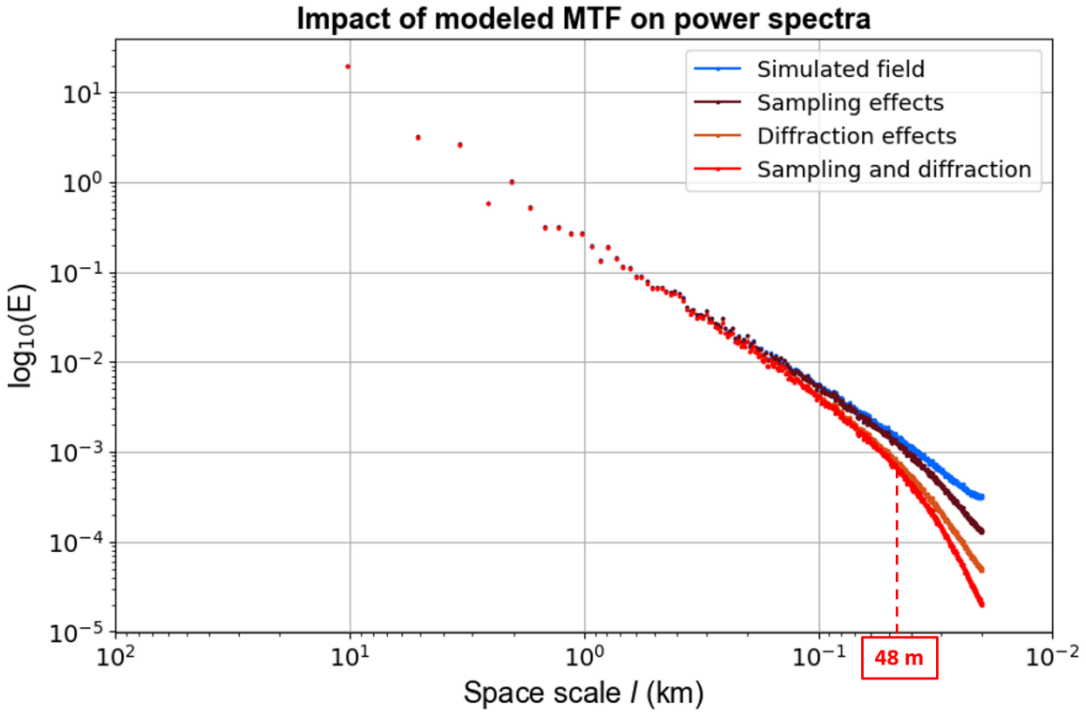

Figure 12: Impact of the Modulation Transfer Function on the power spectra of simulated multifractal fields. The MTF was generated from the analytical model described in Viallefont-Robinet and Léger (2010).

The MTF model used in this study enables to reproduce the impact of the acquisition system on the high frequencies of the image. Although the value of the cut-off frequency was chosen in a more or less arbitrary way, the scale break generated on the original spectrum is similar to that of the fine-scale break l_2 observed on the spectra of our S2 bands. These results provide a physical explanation as to the origin of this fine-scale break, which is the result of the acquisition system, *i.e.* MTF, that reduces spatial variations (smooths the image) at high frequencies inducing a decrease of energy at the finest scales. The strong similarity of the red and light brown curves in Figure 12 suggests that the rupture is mainly related to the diffraction effects of the lens. Further research may be needed to be conclusive of the latter findings by integrating other factors influencing the MTF (electric charge displacements, temperature, etc.). However, the interpretations given here show the potential of power spectra estimators to easily detect the on-orbit effective resolution of the optical sensors, *i.e.* the actual resolution below which any signal will not correctly reflect the spatial properties of the surface.

7 Conclusion and perspectives

In this study, the Universal Multifractal model was applied to analyze the scaling behaviour of Sentinel-2 surface reflectances and optical indexes acquired over the Southwest region of France, and corrected for atmospheric effects by the MAJA processing chain. Images with minimal cloud cover were identified for the whole year 2016 based on the MAJA cloud and shadow detection process. This allowed us to access the dynamics of the scaling properties of surface reflectances, which, to our knowledge, had not yet been explored to date due to the significant impact of clouds on optical data. Different scaling regimes, separated by significant scale breaks, were evidenced from these data. Through the use of multifractal simulations, we could explain the scaling properties and especially the position of scale breaks observed in the images studied by two types of phenomena.

First, a scale break between hundreds of meters and one kilometre was detected that was found to be impacted mostly by the seasonal and geographic specificities of the surface. From this specific break, two scaling regimes with distinct scaling properties were evidenced. Over large extents, reflectances were found to be poorly autocorrelated, revealing spatial properties quite distant from those commonly detected in the phenomena such as topography, rain and clouds. Over small extents, higher autocorrelation were observed in our data, reflecting the presence of multifractal processes comparable to those in turbulence. In addition, a seasonal cycle of scaling parameters was revealed for the fine-scale regime, while no particular temporal behaviour was noticed for the large-scale regime. We showed that this twofold scaling behaviour is directly linked to the physical properties of the surface, and in particular to the agricultural plots that impact its spatial structure. In this way, the fine-scale regime would reflect the *intra-plot* variability governed by multifractal physical and biophysical processes related to crops (soil moisture, vegetation, etc.), while the large-scale regime would represent the *extra-plot* variability resulting from the aggregation of several fine-scale processes which together would not have particular multifractal properties. These interpretations were validated by combining our knowledge of the surface and multifractal simulations, which confirmed that the transition scale between the two observed regimes corresponds to the average size of the agricultural plots for this region.

Second, a singular scaling behaviour was systematically detected at high frequencies on the various optical products: a systematic spectral drop was observed near the resolution of the sensor, reflecting an alteration of the signal measured on fine scales, independently of the observed surface type. This phenomenon was found to be an instrumental artefact generated by the Modulation Transfer Function of the optical system which affects the high frequencies of the acquired image. Therefore, this analysis highlighted the performance limits of the Sentinel-2 optical sensor MSI. The

particular break detected at fine scales (*i.e.* about 40 m scale) would correspond to the *effective resolution* of the sensor, beyond which the fine-scale fractal properties of the observed surface cannot be detected.

To complete the interpretation of the spectral drop artifact observed near the resolution of the sensor, the multi-scale model proposed here could be deepened by integrating other factors influencing the Modulation Transfer Function such as electric charge displacements or temperature. In order to be in the real conditions of Sentinel-2 data acquisition, the real value of cut-off frequency of the MSI sensor could be used in the MTF model. It would also be interesting to establish precisely why the fine-scale break is located at $\sim 4\ l_s$ (mathematical relation) and possibly propose a method to correct this artefact statistically. Here, a fractal stochastic disaggregation could be applied to replace the "impacted" field at fine scales ($l < 4\ l_s$) by a simulated multiplicative cascade that would have the scaling properties of the large-scale field ($l > 4\ l_s$). Based on scaling properties, this type of method preserves the probability distribution from large to fine scales. Such fractal-based techniques have been applied on geophysical variables such as rainfall (Rebora et al., 2006; Sharma et al., 2007; Deidda, 2000; Gires et al., 2012) or soil moisture (Bindlish and Barros, 2002a; Kim and Barros, 2002b; Mascaro et al., 2010). Therefore, it would be interesting to apply this “stochastic” correction to the S2/MAJA surface reflectances and to verify if the spectral drop is still observed near the resolution of the sensor. However, since the disaggregation is based on a random generator, an ensemble of possible fields can be proposed from just one set of scaling parameters. Therefore, this kind of methodology may not be fully suitable in the case of operational hydro-agricultural applications, in particular for determining the position of the extremes. Another possibility to correct the effects of the optical system would be to estimate the original “non-impacted” image from the MTF model proposed in this study. It would simply consist of reversing equation 8, and then estimating the inverse Fourier transform of the field. This solution would respect the deterministic behaviour of the original signal, giving the correct position of the extremes not only statistically valid but also punctually. The challenge would be to get the exact MTF model corresponding to the MSI sensor. Although several methods have been proposed so far to estimate on-orbit MTF (Lei and Tiziani, 1988; Viallefont-Robinet and Léger, 2010; Xu et al., 2014), differences persist between empirical and modelled MTF (Gascon et al., 2017). In the case of an improperly parametrized MTF, this methodology could further alter the signal and generate more scaling artifacts.

This research work demonstrated the potential of the multifractal analysis for spatial characterization of surface reflectances. The theoretical background on which this analysis is based makes it possible to provide an interpretation that is both different and complementary to the more usual texture analysis methods, thus improving our understanding of surface processes and their

spatial heterogeneity. Thanks to the Universal Multifractal model, we were able to identify specific sets of scales ranging from tens of meters to tens of kilometres and on which specific statistical properties were detected. The observed scaling regimes were found to be the results of the combination at different scales of both natural and anthropogenic factors. This spatial characterization could be useful to precisely define the set of scales to consider in information extraction from remote sensing images and help calibrating current surface models which take little account of scaling behaviour, operating on either local or global scales (Ko et al., 2016). It would be possible to verify whether the products synthesized by these models comply with the expected scaling regimes, and if not to constrain the statistics of these models on certain scale ranges. In addition, the present analysis showed that the particular scale ranges detected are directly related to the seasonal (and geographic) specificities of the surface and that these variations should be taken into account in this type of spatial analysis.

Finally, this study showed the potential of multifractal analysis to assess the reliability of satellite products to transcribe what was observed by the sensor. Due to its genericity, the method presented here could be applied to other optical satellite data (Landsat-8, Venμs), even defined at very high resolution (Ikonos). It could also be used to analyze products from different technologies such as radar (Sentinel-1) or passive microwaves (Neuhauser et al., 2019). From a more operational point of view, this could be useful either for the preparation of future space missions in order to determine the capacity of the sensors to detect the inherent scaling properties of the surface processes, or for post-launch assessment to detect in an easy and rapid way the effective resolution of satellite sensors. This methodology complements more usual validation methods enabling a better estimation and understanding of the effective resolution of different products derived from satellite acquisitions.

Acknowledgements

We want to thank O. Hagolle, L. Polidori and M. Ameline for fruitfull discussions and their advice. This study was supported by the “Région Occitanie” (France) and “IUT Paul Sabatier” (Toulouse, France). SM acknowledges the French programs Les Enveloppes Fluides et l’Environnement (LEFE) and Programme National de Télédétection Spatiale (PNTS) of the Institut National de Sciences de l’Univers (INSU-CNRS) for financial support. All the Sentine-2/MAJA products treated in this work were acquired from the French THEIA land data center.

Appendix A: Theory of Multifractals

During the last century researchers realized that many geophysical processes could present scale invariance properties. This was first anticipated by Richardson (1922) in the case of turbulence: he described turbulent flows as cascade processes that transfer kinetic energy from large to small scales. Based on this approach, statistical models of turbulence were proposed such as the famous Kolmogorov law (1941) to describe velocity increments. Later research generalized the study to take into account the heterogeneity of the energy flux (Kolmogorov, 1962; Oboukhov, 1962; Yaglom, 1966). Multi-scale models such as multiplicative cascades were proposed to reproduce scale invariance properties through the use of fractal geometry. Later, scale invariance was noticed in other geophysical fields. For example, in his study of the coast of Britain, Mandelbrot (1967) revealed the presence of fractal properties in topography.

1) *From fractal sets to multifractal fields*

The concept of fractal has been used in many works related to multi-scale analysis and geophysical modelling. Indeed, the term "fractal" refers to any entity (time series or 2D/3D random field) in which each part presents similar properties, geometrically or statistically, to the ensemble. In this manner, the structure of a fractal entity is characterized by scale invariance.

Monofractal stochastic models aim to represent the simple scaling behaviour of geophysical processes. In this context, the fractal dimension or scaling parameter is assumed to be unique, restricting multi-scale modelling to a specific class of variability. However, most geophysical processes are characterized by more complex statistics. In case of operational hydrology, rare and extreme events, present in precipitation or soil moisture for example, correspond to high-order statistics and need to be detected (Hubert et al., 1993). Therefore, multifractal models, characterized by an infinite spectrum of fractal dimensions, have been proposed to account for a more exhaustive set of statistics. Schertzer and Lovejoy (1987), based on the findings of Parisi and Frisch (1985), initially established the multifractal formalism through the fundamental equation:

$$\boldsymbol{Pr}(\oplus_{\lambda} > \boldsymbol{\lambda}^{\gamma}) \approx \boldsymbol{\lambda}^{-c(\gamma)} \quad (9)$$

where $\oplus_{\lambda}$ is a positive normalized random scalar process, time series or random field defined on R^2 or R^3. The symbol "≈" indicates an equality within the limits of slowly varying functions. The mean of the process is assumed to be statistically conserved across scales ($\langle \oplus_{\lambda} \rangle = const$). λ is the observation resolution, here defined as the number of intervals (or pixels) along a dimension of space. Note that the definition given here is different from that usually encountered in remote sensing. In our case, it is

a dimensionless factor that is inversely proportional to the scale l. The latter can be seen as the sampling time or pixel size for time and space domain processes respectively (see Section 3.1 for a more detailed definition of scale and resolution concepts).

Eq.9 expresses the fact that for a multifractal process, the probability of exceeding a threshold varies as a power law of the resolution with exponent $c(\gamma)$. This exponent is called as fractal codimension of the process, depending on the amplitude of thresholds. The thresholds are defined by the following power law:

$$\boldsymbol{T_\lambda = \lambda^\gamma} \quad \textit{10}$$

with γ the notion of singularity, characterizing the amplitude of the process independently of the resolution. Each singularity is associated with a fractal codimension $c(\gamma)$, corresponding to a measure of the sparseness of the area where the process exceeds the thresholds defined by γ. From a more physical point of view, high singularities (detected by high thresholds) are related to rare and extreme events, with high fractal codimensions and inversely low (box-counting) fractal dimensions $D_f(\gamma)$ (Mandelbrot, 1967). Indeed, the latter are related to the dimension of space D through the relation $c(\gamma) = D - D_f(\gamma)$. Therefore, $c(\gamma)$ can be described as a codimension function, increasing with γ, which completely characterizes the multi-scale statistical properties of the field $\bigoplus_\lambda$. In general, if the field is multifractal, $c(\gamma)$ is found to be a convex and positive function (with a fixed point C_1 imposed by the condition of canonical conservation $\langle \bigoplus_\lambda \rangle = const$), whereas monofractality is associated to the trivial case $c(\gamma) = const.$

Since probability distributions and statistical moments are related by a Mellin transform, Schertzer and Lovejoy (1987) proposed an equivalent equation to Eq.9:

$$\langle \bigoplus_\lambda^q \rangle \approx \boldsymbol{\lambda^{K(q)}} \quad \textit{11}$$

where $\langle \cdot \rangle$ is the statistical averaging operator, q is the order of the moment ($q \geq 0$), and $K(q)$ is the moment scaling function. Eq.11 expresses that, for any fixed moment order, statistical moments and resolution are linked through a power law. Singularities and moment orders are directly linked, since the moment scaling function $K(q)$ is the Legendre transform of the codimension function $c(\gamma)$. Similarly to $c(\gamma)$, $K(q)$ is a convex function (with the special case $K(1) = 0$ related to the conservation of the mean across scales), which entirely characterizes the multifractal field.

2) *Multiplicative cascades*

Multiplicative cascades are stochastic models that can be used to build multifractal fields. Cascades are multiplicative processes because they are defined by an iterative multiplicative construction, from larger scales to smaller scales. Considering a two dimensional random signal (field), the cascade consists of dividing each pixel at resolution λ_n (with n the construction level of the cascade) into sub-pixels at finer resolution λ_{n+1}, and then to multiply the latter by a random variable $\mu\varepsilon$. This is described by the following equation:

$$\Phi_{\lambda_{n+1}} = \boldsymbol{\mu\varepsilon} \times \Phi_{\lambda_n} \qquad (12)$$

In this manner, the statistical properties of the field $\Phi_{\lambda_{n+1}}$ are directly related to the statistical properties of the coarser field Φ_{λ_n}. If all the multiplicative random variables used for each step of the iterative construction are independent and identically distributed, and distributed independently of the scale, the final random field (obtained after multiple iterations) presents scale invariant properties.

Several models of cascades have been developed so far. First models were built within the framework of turbulence, such as the α-model (Schertzer and Lovejoy, 1984) which corresponds to discrete construction of cascades: the multiplicative random variables are limited to two possible fixed values, respectively leading to increasing or decreasing pixel value when the resolution is refined. Later, more elaborate models were constructed generalizing the discrete case to continuous cascades (Dubrulle, 1994; Schertzer and Lovejoy, 1987, 1991, 1997; She and Levêque, 1994). The latter are based on an infinite number of steps between any pair of resolutions, leading to continuity in scale. The benefit of continuous cascades is twofold. First, they can represent possibly more realistic structures by avoiding any arbitrary discretization of scales. Moreover, they often converge towards random processes that are characterized by a small number of degrees of freedom (special cases of log-infinitely divisible distributions). This is interesting considering that multifractal fields built by multiplicative cascade processes would otherwise need an infinite number of scaling parameters (one for each fractal dimension). For example, She and Levêque (1994) proposed the Log-Poisson model which constructs multifractal fields from the generation of the random variable $\mu\varepsilon$ whose distribution law is of log-Poisson type. The (log-) Poisson laws are part of the (log-) infinitely-divisible laws, just as the (log-) stable laws (including the Gaussian case). The Universal Multifractal (UM) model proposed by Schertzer and Lovejoy (1987) uses random variables $\mu\varepsilon$ of log-stable laws to generate the multifractal field (see Appendix D for more details on the generation of such a field). In both models, only two fundamental parameters are needed to fully define multifractality, *i.e.* to fully characterize the $c(\gamma)$, $K(q)$ functions.

3) *Universal Multifractals*

Physically, multifractal fields built by Log-Poisson or Log-stable cascades are found in many geophysical applications. The Log-Poisson model has been successfully applied to different geophysical variables such as rain (Deidda, 2000), or even soil moisture (Mascaro et al., 2010). However, the Log-Poisson model can have the disadvantages of representing a somewhat restricted range of variabilities, since they are not suitable for modeling processes with unbounded singularities. On the other hand, by assuming the stability of the random variables and suitable renormalization, the UM model is likely adaptable for characterizing a wide range of processes: topography (Lavallée et al., 1993), rain and clouds (Tessier et al., 1993) and more recently soil moisture and vegetation optical indexes (Lovejoy et al., 2008b). Moreover, a possibly more immediate physical interpretation of the parameters is found in this model. For mathematical and physical arguments supporting the universality of the UM model, see Schertzer and Lovejoy (1997); see also Gupta and Waymire (1997) for discussion about its generality. The UM model defines the moment scaling function using two "universal" parameters, through the following equation (Schertzer and Lovejoy, 1987):

$$\boldsymbol{K(q) = \frac{C_1}{(\alpha - 1)}(q^{\alpha} - q)} \qquad \textit{13}$$

where α is the degree of multifractality of the field. It varies between 0 (monofractality) and 2 (log-normality) and expresses how fast the codimension evolves as a function of the singularity. The second parameter C_1 is the codimension giving the dominant contribution to the mean value of the field (related to moment of order 1): $C_1 = K'(1)$. Physically, it indicates inhomogeneity (dispersion) of the field: it varies from 0 (homogeneous field) to the dimension D of the embedding space (very intermittent field). Because of the Legendre transform, $c(C_1) = K'(1)$ is also defined as the fixed point of the codimension function.

4) *FIF model*

Generally, most geophysical fields are "non-conservative", *i.e.* integrated processes defined by a certain degree of fractional integration (classical integration with non-integer orders). This appellation comes from multifractal cascade models: see Gagnon et al., 2006 for detailed explanations on the notion of fractional integration and its use in 2D multifractal models. Thus, to account for a wider range of processes (like filtered fields caracterized by steeper spectra), an extension of the UM model to non-conservative fields has been proposed (Schertzer and Lovejoy, 1991): the Fractionally Integrated Flux (FIF) model. It expresses the degree of fractional integration of the UM field using a third parameter, H. The latter is called the order of integration and defines the non-conservativity of the field: in plain

words, the larger is H, the smoother is the field. The integrated flux is noted R_λ and is characterized by a power law variation of its stationary increments:

$$\Delta \boldsymbol{R_\lambda} \approx \oplus_{\boldsymbol{\lambda}} \Delta \boldsymbol{x^H} \quad \textit{14}$$

where ΔR_λ are the increments (fluctuations of the flux) estimated over a varying window Δx, which is equivalent to the spatial scale l. Note that when $H = 0$, the equation corresponds to the conservative case $\oplus_\lambda$, and that when $H < 0$ the equation corresponds to the specific "fractional derivation" non-conservative case. Additionally, in the case of two dimensional fluxes, Eq.14 also applies for other directions (*i.e.* Δy increments), with the same exponent H if the process is isotropic.

Appendix B: Estimation of Structure Functions and Statistical Moments

1) *Structure functions: some evidence of non-conservativity*

The structure functions were initially used in turbulence by Kolmogorov (1941) to highlight the scaling behaviour of velocity increments. Then, these methods were widely applied in geophysics, in particular thanks to their simplicity of construction and interpretation. Indeed, unlike the spectrum which implies a transform in the Fourier domain, the structure functions simply represent the fluctuations of the observations in real space, as a function of their distance. In addition, these methods allow direct access to the degree of smoothness (or degree of integration) of the data, also called in the multifractal formalism the "non-conservative" nature of the data studied. This is possible through the estimation of the parameter H that characterizes any integrated multifractal data R_λ. In the multifractal formalism, R_λ is defined by the power law variation of its stationary increments described in Appendix A (Eq.14).

There are several ways to estimate these fluctuations. The simplest is to calculate the average of the absolute differences (or gradient) of R_λ. In general, this method is very suitable for processes characterized by a parameter H between 0 and 1 (Lovejoy and Schertzer, 2012a), thus corresponding to increasing fluctuations with the distance Δx. However, one constraint with this definition is that it does not allow decreasing fluctuations to be represented with distance: for multifractal data defined by $H < 0$, the structure function converges to a constant "parasitic" value, which gives an inaccurate estimate of H (which would be considered equal to 0). To be able to extend the range of H to which the structure functions have access, one solution is to change the shape of the wave estimating the fluctuations. Lovejoy and Schertzer (2012b) proposed a simple formalism of definitions of fluctuations which is based on that of wavelets. In particular, Haar's wavelet is a definition that turns out to be simple to calculate and interpret, while allowing access to negative H values. The fluctuations estimated from this method are calculated according to the following equation:

$$\Delta \boldsymbol{R_\lambda}(\Delta \boldsymbol{x}) = \langle \frac{\mathbf{2}}{\Delta \boldsymbol{x}} \left| \boldsymbol{S}(\boldsymbol{x}) + \boldsymbol{S}(\boldsymbol{x} + \Delta \boldsymbol{x}) - \mathbf{2}\boldsymbol{S}\left(\boldsymbol{x} + \frac{\Delta \boldsymbol{x}}{\mathbf{2}}\right) \right| \rangle \quad (15)$$

where x and Δx are vectors and $\langle \cdot \rangle$ corresponds to the empirical average. S is the cumulative sum of the integrated data R_λ from which the global average has been subtracted. Thus, although this definition seems complex at first glance, it simply consists in estimating the average fluctuations from x to $x + \frac{\Delta x}{2}$ and from $x + \frac{\Delta x}{2}$ to $x + \Delta x$. We can note that, from an algorithmic point of view, equation 8 involves aggregating the field at half the resolution as to allow the calculation of $\frac{\Delta x}{2}$. This implies that, in the case of Haar wavelets, the structure function will not be defined for the finest observation scale.

This technique was used in this study to estimate the structure functions and the corresponding H parameters of our surface S2 products. In particular, in the case of 2D processes, fluctuations were estimated on vertical Δx and horizontal Δy distances separately, allowing us to obtain H_x and H_y parameters respectively. If the observations present indeed multifractal properties and are non-conservative in nature, the order of integration H_x (H_y) should be the slope of the increments ΔR_λ, plotted in a log-log graph as a function of space scale Δx (Δy).

2) *Statistical moments: multifractal properties*

Statistical moments analysis deepens and extends spectral or structure functions analysis by focusing on the extreme variability of the signal. By comparison with the spectral analysis which represents the evolution of a single order of statistics, this method analyzes the behaviour of a set of statistical moments on the range of scales studied.

To test the presence of multifractal properties in the data (Eq.11), statistical moments and moment scaling function need to be estimated. To do this, different steps must be followed. First, the underlying flux $\Phi_{\lambda_{max}}$ has to be reconstructed from the data, *i.e.* random field R, at the maximum observation resolution λ_{max}. Because of the possible existence of a fractional integration of order H (Eq.14), a fractional derivative of the same order should be done. In this study, the modulus of the gradient was applied to the data. Indeed, this operator provides a simple and good numerical approximation of the fractional derivation without prior knowledge of H order (Lavallée et al., 1993; see also Renosh, 2015 for discussion about this approximation):

$$\Phi_{\lambda_{max}} = \sqrt{\left(\frac{\partial R_{\lambda_{max}}}{\partial x}\right)^2 + \left(\frac{\partial R_{\lambda_{max}}}{\partial y}\right)^2} \qquad (16)$$

Once the flux (conservative field) is retrieved, $\Phi_{\lambda_{max}}$ is normalized by its mean.

The second step involves the degradation of the flux at lower resolutions $\lambda < \lambda_{max}$. It aims to approximate the inversion of the stochastic multiplicative cascade by iteratively averaging the flux at coarser scales: each coarse pixel (level n of the cascade) is obtained by a simple average of neighboring finer pixels (level $n+1$). Note that each roughened pixel size is a power of two multiplied greater than the observation scale l_{min} ($= \frac{L}{\lambda_{max}}$).

Finally, empirical moments (*i.e.* computing q-th order moments in Eq.11 while replacing statistical averages by empirical averages) are then computed for various orders and all accessible resolutions. Because of sample size limitations and/or possible divergence of high-order moments (Hubert et al.,

922 2007), in this study moments were computed for orders set from 0 to 3, by steps of 0.1. On a log-log
923 graph, the different moments are plotted as a function of the resolution. If linearity is observed for
924 each moment curve, at least over a significant range of resolutions, Eq.11 is therefore verified, which
925 is the signature of multifractality. The empirical moment scaling function can be estimated, with $K(q)$
926 corresponding to the slope of each linear fit of qth order moment. Afterwards, the universal
927 parameters α and C_1 may be obtained by optimization: here the Nelder-Mead method is used to find
928 the couple of parameters minimizing the (quadratic) distance between the empirical function $K(q)$
929 and the UM model form (Eq.13).

930

Appendix C: Results for mean structure functions and statistical moments

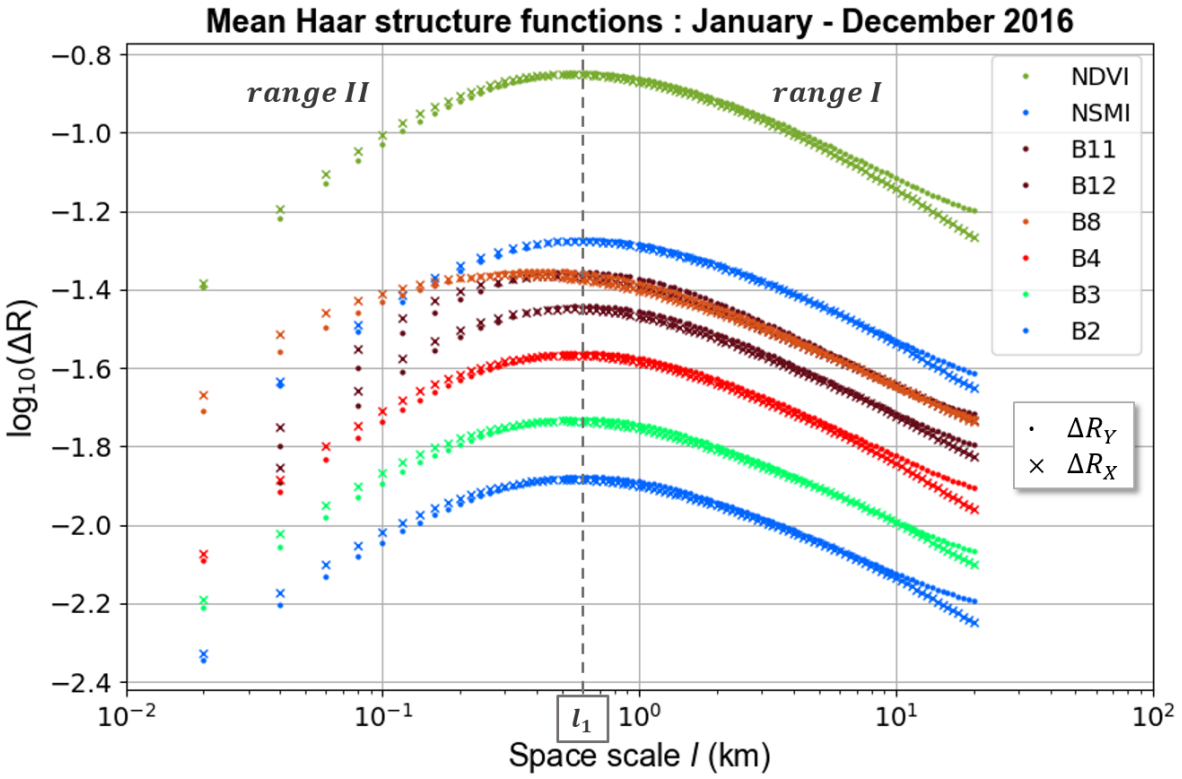

Figure 13: Mean Haar structure functions estimated from Sentinel-2 bands and indexes, over the period January-December 2016. For each band, structure functions are computed in two orthogonal directions (X and Y axis of the image).

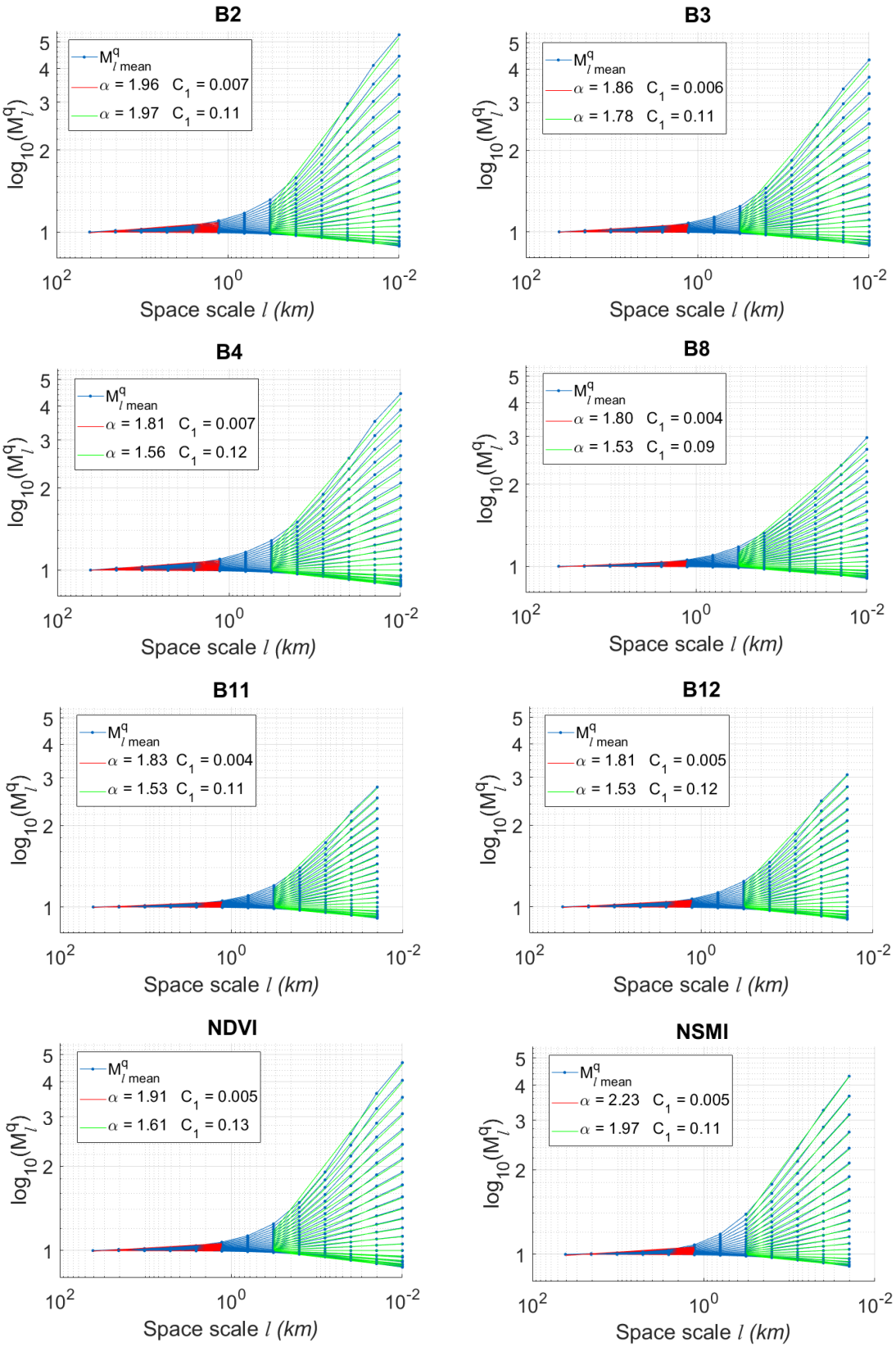

Figure 14: Mean moments estimated from Sentinel-2 bands and indexes, over the period January-December 2016. The straight lines in red and green correspond to the linear regressions carried out respectively on range I (large scales) and range II (small scales).

933

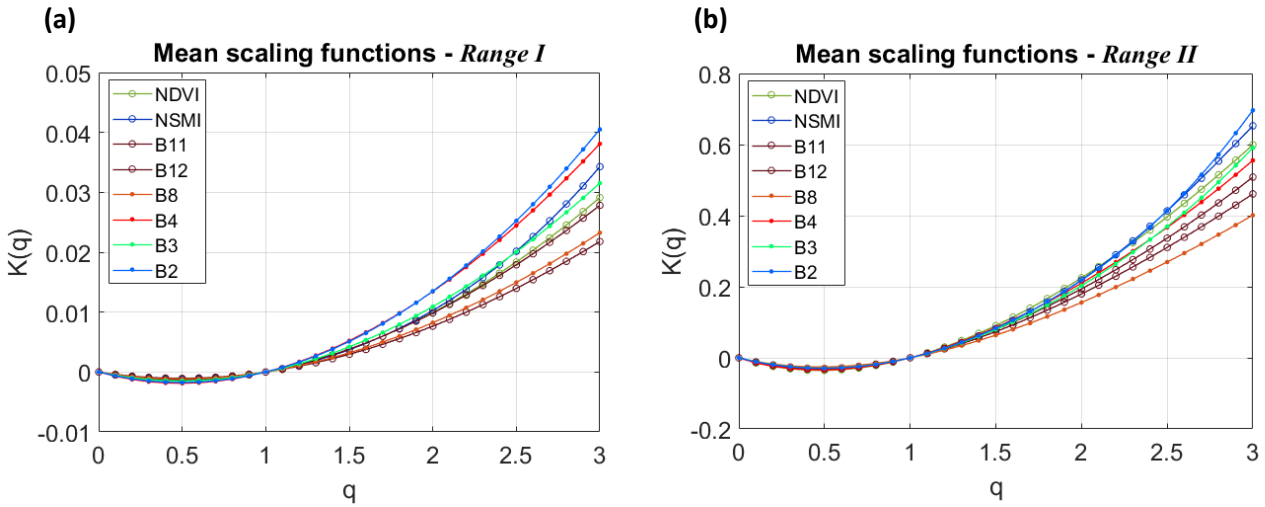

Figure 15: Scaling functions estimated from the mean statistical moments in figure 14, for range I (a) and range II (b). Note the different range of values on the vertical axes.

934

Appendix D: Simulation of multifractal random fields

The simulator that we present here is used to generate multifractal random fields knowing the three parameters α, C_1 and H of the UM model (FIF version) as well as the size of the simulation domain corresponding to the maximum resolution. This simulator includes several steps, which are described in detail in various works on multifractal processes such as Lovejoy and Schertzer (2010b, 2010c), Pecknold et al. (1993), and Verrier (2011). We therefore invite the reader to refer to this work for more information on these processing steps.

In general, this simulator aims to reproduce the mathematical construction of the multiplicative cascades corresponding to the UM/FIF model, defined in Appendix A. This construction is based on five main steps that we describe hereafter:

1) *Generation of the log-stable random variable Υ_α :*

The construction of the UM model is based on the generation of a log-stable random variable, corresponding here to an α-stable white noise Υ_α. The parameter α designates the degree of multifractality of the UM model, and also corresponds to the stability index relating to stable laws (Schertzer et al., 2002). Thus, a first step consists in generating Υ_α thanks to the algorithm of Chambers et al. (1976). This algorithm makes it possible to simulate stable variables quickly and efficiently, simply from realizations of independent random variables and according to uniform and exponential laws. Note here that some additional constraints must be considered to generate Υ_α, relatively to its normalisation (unit asymmetrical α-stable white noise) and its asymmetry (asymmetry parameter set to -1).

2) *Multiplication by the amplitude factor σ :*

The random variable Υ_α is then multiplied by an amplitude factor σ allowing to integrate the parameter C_1 in the construction of the cascade:

$$\boldsymbol{\sigma = \left(\frac{c_1}{|\alpha - 1|}\right)^{\frac{1}{\alpha}}}$$

3) *Generator creation r_λ :*

In order to obtain the multifractal field, we must first construct the random variable r_λ called "generator". This is obtained by convolution of the log-stable variable σ. Υ_α and a filter g_α (in negative power law of the distance) such that:

$$g_{\alpha}(\vec{x}) = \frac{1}{\|\vec{x}\|^{\frac{D}{\alpha}}} \quad (18)$$

where $\|\cdot\|$ designates the Euclidian norm, *i.e.* in the 2D case $\|\vec{x}\| = \|(x,y)\| = \sqrt{x^2+y^2}$. For the sake of speed, the convolution operations present in this simulator are performed numerically in the Fourier domain by means of the two-dimensional fft or "Fast Fourier Transform". D is here taken equal to 2 for a two-dimensional simulation.

4) *Generation of the conservative process* $\oplus_\lambda$ *:*

The conservative process (or flux) is finally obtained by exponentiation of the generator, then normalization:

$$\oplus_\lambda = \frac{e^{\Gamma\lambda}}{\langle e^{\Gamma\lambda}\rangle} \quad (19)$$

5) *Generation of the integrated process* R_λ *:*

In the case of the simulation of a non-conservative process (integrated process named here as "field"), a last step consists in applying a convolution to $\oplus_\lambda$ by the filter in decreasing power law g_H, defined by :

$$g_H(\vec{x}) = \frac{1}{\|\vec{x}\|^{D-H}} \quad (20)$$

This convolution amounts to carrying out a fractional integration of order H (less than D) (Gagnon et al., 2006). In the particular case where $H = 0$, step 5 is omitted since here the random process to be generated is conservative, that is to say $R_\lambda = \oplus_\lambda$.

Appendix E: Modelling of the Modulation Transfer Function of an optical sensor from the characteristics of the lens (diffraction) and detector (sampling)

$$\boldsymbol{MTF} = \boldsymbol{MTF_{diffract}} \times \boldsymbol{MTF_{sampling}}$$

$$\boldsymbol{MTF_{diffract}} = \frac{2}{\Pi}\left\{\cos^{-1}\left(\frac{f}{f_c}\right) - \left(\frac{f}{f_c}\right)\sqrt{1-\left(\frac{f}{f_c}\right)^2}\right\}$$

$$f = \sqrt{{f_x}^2 + {f_y}^2}$$

$$f_c = \frac{a}{\lambda D} \text{ (cut-off frequency)}$$

a : lens diameter

λ : radiation wavelength

D : focal length

$$\boldsymbol{MTF_{sampling}} = sinc\left(\Pi\frac{f_x}{f_s}\right).sinc\left(\Pi\frac{f_y}{f_s}\right)$$

f_s : sampling frequency

References

Aguado, P. L., Del Monte, J. P., Moratiel, R., & Tarquis, A. M. (2014). Spatial Characterization of Landscapes through Multifractal Analysis of DEM. *The Scientific World Journal*, *2014*, 1-9. https://doi.org/10.1155/2014/563038

Alonso, C., Tarquis, A. M., Zúñiga, I., & Benito, R. M. (2017). Spatial and radiometric characterization of multi-spectrum satellite images through multi-fractal analysis. *Nonlinear Processes in Geophysics*, *24*(2), 141-155. https://doi.org/10.5194/npg-24-141-2017

Ameline, M., Fieuzal, R., Betbeder, J., Berthoumieu, J.-F., & Baup, F. (2018). Estimation of Corn Yield by Assimilating SAR and Optical Time Series Into a Simplified Agro-Meteorological Model : From Diagnostic to Forecast. *IEEE Journal of Selected Topics in Applied Earth Observations and Remote Sensing*, *11*(12), 4747-4760. https://doi.org/10.1109/JSTARS.2018.2878502

Bach, H., & Mauser, W. (2003). Methods and examples for remote sensing data assimilation in land surface process modeling. *IEEE Transactions on Geoscience and Remote Sensing*, *41*(7), 1629-1637. https://doi.org/10.1109/TGRS.2003.813270

Battude, M. (2017). *Estimation des rendements, des besoins et consommations en eau du maïs dans le Sud-Ouest de la France : Apport de la télédétection à hautes résolutions spatiale et temporelle*. Université Toulouse 3 Paul Sabatier.

Battude, M., Al Bitar, A., Morin, D., Cros, J., Huc, M., Marais Sicre, C., Le Dantec, V., & Demarez, V. (2016). Estimating maize biomass and yield over large areas using high spatial and temporal resolution Sentinel-2 like remote sensing data. *Remote Sensing of Environment*, *184*, 668-681. https://doi.org/10.1016/j.rse.2016.07.030

Baup, F., Fieuzal, R., Marais-Sicre, C., Dejoux, J.-F., le Dantec, V., Mordelet, P., Claverie, M., Hagolle, O., Lopes, A., Keravec, P., Ceschia, E., Mialon, A., & Kidd, R. (2012). MCM'10 : An experiment for satellite multi-sensors crop monitoring from high to low resolution observations. *2012 IEEE International Geoscience and Remote Sensing Symposium*, 4849-4852. https://doi.org/10.1109/IGARSS.2012.6352527

Baup, Frédéric, Fieuzal, R., & Betbeder, J. (2015). Estimation of soybean yield from assimilated optical and radar data into a simplified agrometeorological model. *Geoscience and Remote Sensing Symposium (IGARSS), 2015 IEEE International*, 3961–3964. http://ieeexplore.ieee.org/abstract/document/7326692/

Benz, U. C., Hofmann, P., Willhauck, G., Lingenfelder, I., & Heynen, M. (2004). Multi-resolution, object-oriented fuzzy analysis of remote sensing data for GIS-ready information. *ISPRS Journal of Photogrammetry and Remote Sensing*, *58*(3-4), 239-258. https://doi.org/10.1016/j.isprsjprs.2003.10.002

Betbeder, J., Fieuzal, R., & Baup, F. (2016). Assimilation of LAI and Dry Biomass Data From Optical and SAR Images Into an Agro-Meteorological Model to Estimate Soybean Yield. *IEEE Journal of Selected Topics in Applied Earth Observations and Remote Sensing*, *9*(6), 2540-2553. https://doi.org/10.1109/JSTARS.2016.2541169

Béziat, P., Ceschia, E., & Dedieu, G. (2009). Carbon balance of a three crop succession over two cropland sites in South West France. *Agricultural and Forest Meteorology*, *149*(10), 1628-1645. https://doi.org/10.1016/j.agrformet.2009.05.004

Bindlish, R., & Barros, A. P. (2002). Subpixel variability of remotely sensed soil moisture : An inter-comparison study of SAR and ESTAR. *IEEE Transactions on Geoscience and Remote Sensing*, *40*(2), 326-337. https://doi.org/10.1109/36.992792

Burel, E. (2018). *Modélisation des hétérogénéités de la réserve utile et du développement des cultures au sein d'un sous-bassin versant en Midi-Pyrénées*. Université Toulouse 3 Paul Sabatier.

Carnahan, W. H., & Zhou, G. (1986). *Fourier transform techniques for the evaluation of the Thematic Mapper line spread function*.

Chambers, J. M., Mallows, C. L., & Stuck, B. W. (1976). A method for simulating stable random variables. *Journal of the american statistical association*, *71*(354), 340-344.

Chen, Y., & Wang, J. (2013). Multifractal characterization of urban form and growth : The case of Beijing. *Environment and Planning B: Planning and Design*, *40*(5), 884-904. https://doi.org/10.1068/b36155

Cheng, Q., Russell, H., Sharpe, D., Kenny, F., & Qin, P. (2001). GIS-based statistical and fractal/multifractal analysis of surface stream patterns in the Oak Ridges Moraine. *Computers & Geosciences*, *27*(5), 513-526. https://doi.org/10.1016/S0098-3004(00)00112-6

Choi, T. (2002). *KONOS satellite on orbit modulation transfer function (MTF) measurement using edge and pulse method* [Electrical Engineering Department]. South Dakota State University.

Claverie, M., Demarez, V., Duchemin, B., Hagolle, O., Ducrot, D., Marais-Sicre, C., Dejoux, J.-F., Huc, M., Keravec, P., Béziat, P., Fieuzal, R., Ceschia, E., & Dedieu, G. (2012). Maize and sunflower biomass estimation in southwest France using high spatial and temporal resolution remote sensing data. *Remote Sensing of Environment*, *124*, 844-857. https://doi.org/10.1016/j.rse.2012.04.005

De Cola, L. (1989). Fractal Analysis of a Classified Landscape Scene. *Photogrammetric Engineering and Remote Sensing*, *55*(5), 601-610.

Deidda, R. (2000). Rainfall downscaling in a space-time multifractal framework. *Water Resources Research*, *36*(7), 1779-1794. https://doi.org/10.1029/2000WR900038

Dejoux, J.-F., Dedieu, G., Hagolle, O., Ducrot, D., Menaut, J.-C., Ceschia, E., Baup, F., Demarez, V., Marais-Sicre, C., Kadiri, M., & Gascoin, S. (2012). *Kalideos OSR MiPy : Un observatoire pour la recherche et la démonstration des applications de la télédétection à la gestion des territoires*. 16.

D'Errico, J. (2017). *Shape Language Modelling*. https://fr.mathworks.com/matlabcentral/fileexchange/24443-slm-shape-language-modeling

Dubrulle, B. (1994). Intermittency in fully developed turbulence : Log-Poisson statistics and generalized scale covariance. *Physical review letters*, *73*(7), 959.

Fieuzal, R., Marais Sicre, C., & Baup, F. (2017). Estimation of corn yield using multi-temporal optical and radar satellite data and artificial neural networks. *International Journal of Applied Earth Observation and Geoinformation*, *57*, 14-23. https://doi.org/10.1016/j.jag.2016.12.011

Fieuzal, Rémy, & Baup, F. (2015). Estimation of sunflower yield using multi-spectral satellite data (optical or radar) in a simplified agro-meteorological model. *Geoscience and Remote Sensing Symposium (IGARSS), 2015 IEEE International*, 4001–4004. http://ieeexplore.ieee.org/abstract/document/7326702/

Fieuzal, Rémy, Baup, F., & Marais-Sicre, C. (2013). Monitoring Wheat and Rapeseed by Using Synchronous Optical and Radar Satellite Data—From Temporal Signatures to Crop Parameters Estimation. *Advances in Remote Sensing*, *02*(02), 162-180. https://doi.org/10.4236/ars.2013.22020

Fraser, R., & Kaufman, Y. (1985). The Relative Importance of Aerosol Scattering and Absorption in Remote Sensing. *IEEE Transactions on Geoscience and Remote Sensing*, *GE-23*(5), 625-633. https://doi.org/10.1109/TGRS.1985.289380

Gagnon, J.-S., Lovejoy, S., & Schertzer, D. (2006). Multifractal earth topography. *Nonlinear Processes in Geophysics*, *13*(5), 541–570.

Gascon, F., Bouzinac, C., Thépaut, O., Jung, M., Francesconi, B., Louis, J., Lonjou, V., Lafrance, B., Massera, S., Gaudel-Vacaresse, A., Languille, F., Alhammoud, B., Viallefont, F., Pflug, B., Bieniarz, J., Clerc, S., Pessiot, L., Trémas, T., Cadau, E., … Fernandez, V. (2017). Copernicus Sentinel-2A Calibration and Products Validation Status. *Remote Sensing*, *9*(6), 584. https://doi.org/10.3390/rs9060584

Gatti, A., & Naud, C. (2017). *Sentinel-2 Products Specification Document*. 487.

Gires, A., Onof, C., Maksimovic, C., Schertzer, D., Tchiguirinskaia, I., & Simoes, N. (2012). Quantifying the impact of small scale unmeasured rainfall variability on urban runoff through multifractal downscaling : A case study. *Journal of Hydrology*, *442-443*, 117-128. https://doi.org/10.1016/j.jhydrol.2012.04.005

Gupta, V. K., & Waymire, E. C. (1997). Reply-Universal Multifractals Do Exist! : Comments on A Statistical Analysis of Mesoscale Rainfall as a Random Cascade. *Journal of Applied Meteorology*, *36*(9), 1304-1307.

Gustafson, E. J. (1998). Quantifying Landscape Spatial Pattern : What Is the State of the Art? *Ecosystems*, *1*(2), 143-156.

Gutman, G., Byrnes, R., Masek, J., Covington, S., Justice, C., Franks, S., & Headley, R. (2008). Towards monitoring Land-cover and land-use changes at a global scale : The global land survey. *Photogrammetric Engineering & Remote Sensing*, *74*, 6-10.

Hagolle, O., Huc, M., Pascual, D. V., & Dedieu, G. (2010). A multi-temporal method for cloud detection, applied to FORMOSAT-2, VENµS, LANDSAT and SENTINEL-2 images. *Remote Sensing of Environment*, *114*(8), 1747-1755. https://doi.org/10.1016/j.rse.2010.03.002

Hagolle, Olivier, Huc, M., Villa Pascual, D., & Dedieu, G. (2015). A Multi-Temporal and Multi-Spectral Method to Estimate Aerosol Optical Thickness over Land, for the Atmospheric Correction of FormoSat-2, LandSat, VENµS and Sentinel-2 Images. *Remote Sensing*, *7*(3), 2668-2691. https://doi.org/10.3390/rs70302668

Hansen, M., Dubayah, R., & Defries, R. (1996). Classification trees : An alternative to traditional land cover classifiers. *International Journal of Remote Sensing*, *17*(5), 1075-1081. https://doi.org/10.1080/01431169608949069

Huang, C., Goward, S. N., Masek, J. G., Thomas, N., Zhu, Z., & Vogelmann, J. E. (2010). An automated approach for reconstructing recent forest disturbance history using dense Landsat time series stacks. *Remote Sensing of Environment*, *114*(1), 183-198. https://doi.org/10.1016/j.rse.2009.08.017

Hubert, P., Tchiguirinskaia, I., Schertzer, D., Bendjoudi, H., & Lovejoy, S. (2007). Predetermination of floods. *Extreme Hydrological EventsEvents: New Concepts for Security*, *78*, 185-198.

Hubert, P., Tessier, Y., Lovejoy, S., Schertzer, D., Schmitt, F., Ladoy, P., Carbonnel, J. P., Violette, S., & Desurosne, I. (1993). Multifractals and Extreme Rainfall Events. *Geophysical Research Letters*, *20*(10), 931-934. https://doi.org/10.1029/93GL01245

Justice, C. O., Vermote, E., Townshend, J. R. G., Defries, R., Roy, D. P., Hall, D. K., Salomonson, V. V., Privette, J. L., Riggs, G., Strahler, A., Lucht, W., Myneni, R. B., Knyazikhin, Y., Running, S. W., Nemani, R. R., Zhengming Wan, Huete, A. R., van Leeuwen, W., Wolfe, R. E., … Barnsley, M. J. (1998). The Moderate Resolution Imaging Spectroradiometer (MODIS) : Land remote sensing for global change research. *IEEE Transactions on Geoscience and Remote Sensing*, *36*(4), 1228-1249. https://doi.org/10.1109/36.701075

Kim, G., & Barros, A. P. (2002a). Space–time characterization of soil moisture from passive microwave remotely sensed imagery and ancillary data. *Remote Sensing of Environment*, *81*(2-3), 393-403. https://doi.org/10.1016/S0034-4257(02)00014-7

Kim, G., & Barros, A. P. (2002b). Downscaling of remotely sensed soil moisture with a modified fractal interpolation method using contraction mapping and ancillary data. *Remote Sensing of Environment*, *83*(3), 400–413.

King, M. D., Kaufman, Y. J., Tanré, D., & Nakajima, T. (1999). Remote Sensing of Tropospheric Aerosols from Space : Past, Present, and Future. *Bulletin of the American Meteorological society*, *80*(11), 2229-2260.

Ko, A., Mascaro, G., & Vivoni, E. R. (2016). Irrigation Impacts on Scaling Properties of Soil Moisture and the Calibration of a Multifractal Downscaling Model. *IEEE Transactions on Geoscience and Remote Sensing*, *54*(6), 3128-3142. https://doi.org/10.1109/TGRS.2015.2511628

Kolmogorov, A. N. (1962). A refinement of previous hypotheses concerning the local structure of turbulence in a viscous incompressible fluid at high Reynolds number. *Journal of Fluid Mechanics*, *13*(01), 82. https://doi.org/10.1017/S0022112062000518

Kolmogorov, A. N. (1941). The local structure of turbulence in incompressible viscous fluid for very large Reynolds numbers. *Dokl. Akad. Nauk SSSR*, *30*, 299–303.

Lam, N. S.-N. (1990). Description and Measurement of Landsat TM Images Using Fractals. *Photogrammetric Engineering and Remote Sensing*, *56*, 187-195.

Lampkin, D. J., & Yool, S. R. (2004). Monitoring mountain snowpack evolution using near-surface optical and thermal properties. *Hydrological Processes*, *18*(18), 3527-3542. https://doi.org/10.1002/hyp.5797

Lavallée, D., Lovejoy, S., Schertzer, D., & Ladoy, P. (1993). Nonlinear variability of landscape topography : Multifractal analysis and simulation. In *Fractals in Geography* (Prentice Hall, p. 158-192). Eds. Nina Siu-Ngan Lam and Lee De Cola.

Lei, F., & Tiziani, H. J. (1988). A Comparison of Methods to Measure the Modulation Transfer Function of Aerial Survey Lens Systems from the Image Structures. *PHOTOGRAMMETRIC ENGINEERING*, 6.

Lenoble, J., Herman, M., Deuzé, J. L., Lafrance, B., Santer, R., & Tanré, D. (2007). A successive order of scattering code for solving the vector equation of transfer in the earth's atmosphere with aerosols. *Journal of Quantitative Spectroscopy and Radiative Transfer*, *107*(3), 479-507. https://doi.org/10.1016/j.jqsrt.2007.03.010

Liang, S., Fang, H., & Chen, M. (2001). Atmospheric correction of Landsat ETM+ land surface imagery. I. Methods. *IEEE Transactions on Geoscience and Remote Sensing*, *39*(11), 2490-2498. https://doi.org/10.1109/36.964986

Lovejoy, S., & Schertzer, D. (2010a). Towards a new synthesis for atmospheric dynamics : Space–time cascades. *Atmospheric Research*, *96*(1), 1-52. https://doi.org/10.1016/j.atmosres.2010.01.004

Lovejoy, S., & Schertzer, D. (2010b). On the simulation of continuous in scale universal multifractals, part I : Spatially continuous processes. *Computers & Geosciences*, *36*(11), 1393-1403. https://doi.org/10.1016/j.cageo.2010.04.010

Lovejoy, S., & Schertzer, D. (2010c). On the simulation of continuous in scale universal multifractals, Part II : Space–time processes and finite size corrections. *Computers & Geosciences*, *36*(11), 1404-1413. https://doi.org/10.1016/j.cageo.2010.07.001

Lovejoy, S., & Schertzer, D. (2012a). Low-Frequency Weather and the Emergence of the Climate. In A. S. Sharma, A. Bunde, V. P. Dimri, & D. N. Baker (Éds.), *Geophysical Monograph Series* (Vol. 196, p. 231-254). American Geophysical Union. https://doi.org/10.1029/2011GM001087

Lovejoy, S., & Schertzer, D. (2012b). Haar wavelets, fluctuations and structure functions : Convenient choices for geophysics. *Nonlinear Processes in Geophysics*, *19*(5), 513-527. https://doi.org/10.5194/npg-19-513-2012

1175 Lovejoy, S., Schertzer, D., Lilley, M., Strawbridge, K. B., & Radkevich, A. (2008a). Scaling turbulent atmospheric
1176 stratification. I : Turbulence and waves. *Quarterly Journal of the Royal Meteorological Society*,
1177 *134*(631), 277-300. https://doi.org/10.1002/qj.201

1178 Lovejoy, S., Schertzer, D., & Stanway, J. D. (2001). Direct Evidence of Multifractal Atmospheric Cascades from
1179 Planetary Scales down to 1 km. *Physical Review Letters*, *86*(22), 5200-5203.
1180 https://doi.org/10.1103/PhysRevLett.86.5200

1181 Lovejoy, S., Tarquis, A. M., Gaonac'h, H., & Schertzer, D. (2008b). Single-and multiscale remote sensing
1182 techniques, multifractals, and MODIS-derived vegetation and soil moisture. *Vadose Zone Journal*, *7*(2),
1183 533–546.

1184 Lu, D., & Weng, Q. (2007). A survey of image classification methods and techniques for improving classification
1185 performance. *International Journal of Remote Sensing*, *28*(5), 823-870.
1186 https://doi.org/10.1080/01431160600746456

1187 Lyu, C., Cheng, Q., Zuo, R., & Wang, X. (2017). Mapping spatial distribution characteristics of lineaments
1188 extracted from remote sensing image using fractal and multifractal models. *Journal of Earth Science*,
1189 *28*(3), 507-515.

1190 Mandelbrot, B. (1967). How long is the coast of Britain ? Statistical self-similarity and fractional dimension.
1191 *Science*, *156*(3775), 636-638.

1192 Mandelbrot, B. B. (1975). Stochastic models for the Earth's relief, the shape and the fractal dimension of the
1193 coastlines, and the number-area rule for islands. *Proceedings of the National Academy of Sciences*,
1194 *72*(10), 3825-3828. https://doi.org/10.1073/pnas.72.10.3825

1195 Mandelbrot, BENOIT B., & Van Ness, J. W. (1968). Fractional Brownian motions, fractional. *Geophys. Res. Lett*,
1196 *24*, 2099–2102.

1197 Mangiarotti, S., Drapeau, L., & Letellier, C. (2014). Two chaotic global models for cereal crops cycles observed
1198 from satellite in northern Morocco. *Chaos: An Interdisciplinary Journal of Nonlinear Science*, *24*(2),
1199 023130.

1200 Mangiarotti, S., Mazzega, P., Hiernaux, P., & Mougin, E. (2010). The Vegetation dynamics in West Africa from
1201 AVHRR-NDVI data : Horizons of predictability versus spatial scales. *Remote Sensing of Environment*,
1202 *114*(9), 2036-2047.

1203 Mangiarotti, S., Mazzega, P., Hiernaux, P., & Mougin, E. (2012). Predictability of vegetation cycles over the
1204 semi-arid region of Gourma (Mali) from forecasts of AVHRR-NDVI signals. *Remote Sensing of*
1205 *Environment*, *123*, 246-257. https://doi.org/10.1016/j.rse.2012.03.011

1206 Mangiarotti, S., Mazzega, P., Jarlan, L., Mougin, E., Baup, F., & Demarty, J. (2008). Evolutionary Bi-objective
1207 Optimization of a Semi-Arid Vegetation Model with Satellite Data. *Remote Sensing of Environment*,
1208 *112*(4), 1365-1380.

1209 Mangiarotti, S., Sharma, A. K., Corgne, S., Hubert-Moy, L., Ruiz, L., Sekhar, M., & Kerr, Y. (2018). Can the global
1210 modeling technique be used for crop classification? *Chaos, Solitons & Fractals*, *106*, 363-378.
1211 https://doi.org/10.1016/j.chaos.2017.12.003

1212 Manivasagam, V. S., Kaplan, G., & Rozenstein, O. (2019). Developing Transformation Functions for VENμS and
1213 Sentinel-2 Surface Reflectance over Israel. *Remote Sensing*, *11*(14), 1710.
1214 https://doi.org/10.3390/rs11141710

1215 Martimort, P., Arino, O., Berger, M., Biasutti, R., Carnicero, B., Del Bello, U., Fernandez, V., Gascon, F., Greco, B.,
1216 Silvestrin, P., Spoto, F., & Sy, O. (2007). Sentinel-2 optical high resolution mission for GMES operational
1217 services. *2007 IEEE International Geoscience and Remote Sensing Symposium*, 2677-2680.
1218 https://doi.org/10.1109/IGARSS.2007.4423394

Mascaro, G., Vivoni, E. R., & Deidda, R. (2010). Downscaling soil moisture in the southern Great Plains through a calibrated multifractal model for land surface modeling applications : DOWNSCALING SOIL MOISTURE IN THE GREAT PLAINS. *Water Resources Research*, *46*(8). https://doi.org/10.1029/2009WR008855

Neuhauser, M., Verrier, S., Merlin, O., Molero, B., Suere, C., & Mangiarotti, S. (2019). Multi-scale statistical properties of disaggregated SMOS soil moisture products in Australia. *Advances in Water Resources*, 18. https://doi.org/10.1016/j.advwatres.2019.103426

Norton, C. L., Brooks, G. C., & Welch, R. (1977). Optical and Modulation Transfer Function. *Photogrammetric Engineering and Remote Sensing*, *43*, 613-636.

Oboukhov, A. M. (1962). Some specific features of atmospheric tubulence. *Journal of Fluid Mechanics*, *13*(01), 77. https://doi.org/10.1017/S0022112062000506

Pal, M. (2005). Random forest classifier for remote sensing classification. *International Journal of Remote Sensing*, *26*(1), 217-222. https://doi.org/10.1080/01431160412331269698

Paola, J. D., & Schowengerdt, R. A. (1995). A review and analysis of backpropagation neural networks for classification of remotely-sensed multi-spectral imagery. *International Journal of Remote Sensing*, *16*(16), 3033-3058. https://doi.org/10.1080/01431169508954607

Parisi, G., & Frisch, U. (1985). A multifractal model of intermittency. *Turbulence and Predictability in Geophysical Fluid Dynamics and Climate Dynamics*, *84-88*.

Pecknold, S., Lovejoy, S., Schertzer, D., Hooge, C., & Malouin, J. F. (1993). *The simulation of universal multifractals*.

Puissant, A., Hirsch, J., & Weber, C. (2005). The utility of texture analysis to improve per-pixel classification for high to very high spatial resolution imagery. *International Journal of Remote Sensing*, *26*(4), 733-745. https://doi.org/10.1080/01431160512331316838

Qiu, H.-L., Lam, N. S.-N., Quattrochi, D., & Gamon, A. J. (1999). Fractal characterization of hyperspectral imagery. *Photogrammetric Engineering and Remote Sensing*, *65*, 63-71.

Rahman, H., & Dedieu, G. (1994). SMAC : A simplified method for the atmospheric correction of satellite measurements in the solar spectrum. *International Journal of Remote Sensing*, *15*(1), 123-143. https://doi.org/10.1080/01431169408954055

Ramstein, G., & Raffy, M. (1989). Analysis of the structure of radiometric remotely-sensed images. *International Journal of Remote Sensing*, *10*(6), 1049-1073. https://doi.org/10.1080/01431168908903944

Rebora, N., Ferraris, L., Von Hardenberg, J., & Provenzale, A. (2006). Rainfall downscaling and flood forecasting : A case study in the Mediterranean area. *Natural Hazards and Earth System Science*, *6*(4), 611–619.

Reichenbach, S. E. (1991). Characterizing digital image acquisition devices. *Optical Engineering*, *30*(2), 170. https://doi.org/10.1117/12.55783

Renosh, P. R. (2015). *Characterisation of the coupling between oceanic turbulence and the variability of the coastal waters optical properties, using in situ measurements and satellite data* [Université Lille 1 Sciences et Technologies]. http://search.proquest.com/openview/e82d9e0f7d9042460290440064b0c107/1?pq-origsite=gscholar&cbl=54809

Richardson, L. F. (1922). Weather prediction by numerical process. *Cambridge Univ. Press.*

Richter, R., Schläpfer, D., & Müller, A. (2006). An automatic atmospheric correction algorithm for visible/NIR imagery. *International Journal of Remote Sensing*, *27*(10), 2077-2085. https://doi.org/10.1080/01431160500486690

Rodríguez-Fernández, N., de Rosnay, P., Albergel, C., Richaume, P., Aires, F., Prigent, C., & Kerr, Y. (2019). *SMOS Neural Network Soil Moisture Data Assimilation in a Land Surface Model and Atmospheric Impact*. 23.

Rouquié, B., Hagolle, O., Bréon, F.-M., Boucher, O., Desjardins, C., & Rémy, S. (2017). Using Copernicus Atmosphere Monitoring Service Products to Constrain the Aerosol Type in the Atmospheric Correction Processor MAJA. *Remote Sensing*, *9*(12), 1230. https://doi.org/10.3390/rs9121230

Roy, D. P., Wulder, M. A., Loveland, T. R., C.E., W., Allen, R. G., Anderson, M. C., Helder, D., Irons, J. R., Johnson, D. M., Kennedy, R., Scambos, T. A., Schaaf, C. B., Schott, J. R., Sheng, Y., Vermote, E. F., Belward, A. S., Bindschadler, R., Cohen, W. B., Gao, F., … Zhu, Z. (2014). Landsat-8 : Science and product vision for terrestrial global change research. *Remote Sensing of Environment*, *145*, 154-172. https://doi.org/10.1016/j.rse.2014.02.001

Schertzer, D., & Lovejoy, S. (1984). On the Dimension of Atmospheric motions. *Turbulence and Chaotic phenomena in Fluids*, 505-512.

Schertzer, D., & Lovejoy, S. (1987). Physical modeling and analysis of rain and clouds by anisotropic scaling multiplicative processes. *Journal of Geophysical Research*, *92*(D8), 9693. https://doi.org/10.1029/JD092iD08p09693

Schertzer, D., & Lovejoy, S. (1991). Nonlinear geodynamical variability : Multiple singularities, universality and observables. *Non-Linear Variability in Geophysics*, 41-82.

Schertzer, D., & Lovejoy, S. (1997). Universal multifractals do exist! : Comments on "A statistical analysis of mesoscale rainfall as a random cascade". *Journal of Applied Meteorology*, *36*(9), 1296–1303.

Schertzer, D., Lovejoy, S., & Hubert, P. (2002). An introduction to stochastic multifractal fields. *ISFMA Symposium on Environmental Science and Engineering with related Mathematical Problems*, 106–179. http://132.206.6.11/~gang/eprints/Paris.eprints/Stochastic.multi.eprint2002.pdf

Schmitt, F. (1993). Estimation of universal multifractal indices for atmospheric turbulent velocity fileds. *Fractals*, *1*(3), 568-575.

Sharma, D. (2007). Spatial disaggregation of bias-corrected GCM precipitation for improved hydrologic simulation : Ping River Basin, Thailand. *Hydrol. Earth Syst. Sci.*, 19.

She, Z.-S., & Leveque, E. (1994). Universal Scaling Laws in Fully Developed Turbulence. *Physical review letters*, *72*(3).

Siebesma, A. P., & Jonker, H. J. J. (2000). Anomalous Scaling of Cumulus Cloud Boundaries. *Physical Review Letters*, *85*(1), 214-217. https://doi.org/10.1103/PhysRevLett.85.214

Stoian, A., Poulain, V., Inglada, J., Poughon, V., & Derksen, D. (2019). Land Cover Maps Production with High Resolution Satellite Image Time Series and Convolutional Neural Networks : Adaptations and Limits for Operational Systems. *Remote Sensing*, *11*(17), 1986. https://doi.org/10.3390/rs11171986

Tallec, T., Béziat, P., Jarosz, N., Rivalland, V., & Ceschia, E. (2013). Crops' water use efficiencies in temperate climate : Comparison of stand, ecosystem and agronomical approaches. *Agricultural and Forest Meteorology*, *168*, 69-81. https://doi.org/10.1016/j.agrformet.2012.07.008

Tan, X., Huang, B., Batty, M., & Li, J. (2021). Urban Spatial Organization, Multifractals, and Evolutionary Patterns in Large Cities. *Annals of the American Association of Geographers*, *111*(5), 1539-1558.

Tessier, Y., Lovejoy, S., & Schertzer, D. (1993). *Universal Multifractals : Theory and Observations for Rain and Clouds*. https://doi.org/10.1175/1520-0450

Tucker, C. J., & Sellers, P. J. (1986). Satellite remote sensing of primary production. *International Journal of Remote Sensing*, *7*(11), 1395-1416. https://doi.org/10.1080/01431168608948944

Vermote, E. F., Tanre, D., Deuze, J. L., Herman, M., & Morcette, J.-J. (1997). Second Simulation of the Satellite Signal in the Solar Spectrum, 6S : An overview. *IEEE Transactions on Geoscience and Remote Sensing*, *35*(3), 675-686. https://doi.org/10.1109/36.581987

Verrier, S. (2011). *Modélisation de la variabilité spatiale et temporelle des précipitations à la sub-mésoéchelle par une approche multifractale* [Université de Versailles-Saint Quentin en Yvelines]. https://hal-sde.archives-ouvertes.fr/tel-00734327/

Verrier, S. (2020). Multifractal and multiscale entropy scaling of in-situ soil moisture time series : Study of SMOSMANIA network data, southwestern France. *Journal of Hydrology*, *585*, 124821. https://doi.org/10.1016/j.jhydrol.2020.124821

Viallefont-Robinet, F., & Léger, D. (2010). Improvement of the edge method for on-orbit MTF measurement. *Optics Express*, *18*(4), 3531. https://doi.org/10.1364/OE.18.003531

Weszka, J. S., Dyer, C. R., & Rosenfeld, A. (1976). A Comparative Study of Texture Measures for Terrain Classification. *IEEE Transactions on Systems, Man, and Cybernetics*, *SMC-6*(4), 269-285. https://doi.org/10.1109/TSMC.1976.5408777

Yaglom, A. M. (1966). The influence of fluctuations in energy dissipation on the shape of turbulence characteristics in the inertial interval. *Soviet Physics Doklady*, *11*, 26.

Zucker, S. W. (1976). Region growing : Childhood and adolescence. *Computer Graphics and Image Processing*, *5*(3), 382-399. https://doi.org/10.1016/S0146-664X(76)80014-7

List of figures

List of tables